Monthly Notices
of the
ROYAL ASTRONOMICAL SOCIETY

MNRAS **458,** 4025–4043 (2016)
Advance Access publication 2016 March 7

doi:10.1093/mnras/stw522

# WASP-121 b: a hot Jupiter close to tidal disruption transiting an active F star

L. Delrez,[1]★ A. Santerne,[2] J.-M. Almenara,[3,4] D. R. Anderson,[5] A. Collier-Cameron,[6] R. F. Díaz,[7] M. Gillon,[1] C. Hellier,[5] E. Jehin,[1] M. Lendl,[8,7] P. F. L. Maxted,[5] M. Neveu-VanMalle,[7,9] F. Pepe,[7] D. Pollacco,[10] D. Queloz,[9,7] D. Ségransan,[7] B. Smalley,[5] A. M. S. Smith,[11,5] A. H. M. J. Triaud,[12,13,7]† S. Udry,[7] V. Van Grootel[1] and R. G. West[10]

[1]*Institut d'Astrophysique et Géophysique, Université de Liège, allée du 6 Août 17, B-4000 Liège, Belgium*
[2]*Instituto de Astrofísica e Ciências do Espaço, Universidade do Porto, CAUP, Rua das Estrelas, PT-4150-762 Porto, Portugal*
[3]*Univ. Grenoble Alpes, IPAG, F-38000 Grenoble, France*
[4]*CNRS, IPAG, F-38000 Grenoble, France*
[5]*Astrophysics Group, Keele University, Staffordshire ST5 5BG, UK*
[6]*SUPA, School of Physics and Astronomy, University of St. Andrews, North Haugh, Fife KY16 9SS, UK*
[7]*Observatoire de Genève, Université de Genève, 51 Chemin des Maillettes, CH-1290 Sauverny, Switzerland*
[8]*Space Research Institute, Austrian Academy of Sciences, Schmiedlstr. 6, A-8042 Graz, Austria*
[9]*Cavendish Laboratory, Department of Physics, University of Cambridge, JJ Thomson Avenue, Cambridge CB3 0HE, UK*
[10]*Department of Physics, University of Warwick, Coventry CV4 7AL, UK*
[11]*N. Copernicus Astronomical Centre, Polish Academy of Sciences, Bartycka 18, PL-00-716 Warsaw, Poland*
[12]*Centre for Planetary Sciences, University of Toronto at Scarborough, 1265 Military Trail, Toronto, ON M1C 1A4, Canada*
[13]*Department of Astronomy & Astrophysics, University of Toronto, Toronto, ON M5S 3H4, Canada*

Accepted 2016 March 1. Received 2016 March 1; in original form 2015 June 8

## ABSTRACT

We present the discovery by the WASP-South survey of WASP-121 b, a new remarkable short-period transiting hot Jupiter. The planet has a mass of $1.183^{+0.064}_{-0.062}$ $M_{\rm Jup}$, a radius of $1.865 \pm 0.044$ $R_{\rm Jup}$, and transits every $1.274\,9255^{+0.000\,0020}_{-0.000\,0025}$ days an active F6-type main-sequence star ($V = 10.4$, $1.353^{+0.080}_{-0.079}$ $M_\odot$, $1.458 \pm 0.030$ $R_\odot$, $T_{\rm eff} = 6460 \pm 140$ K). A notable property of WASP-121 b is that its orbital semimajor axis is only ∼1.15 times larger than its Roche limit, which suggests that the planet is close to tidal disruption. Furthermore, its large size and extreme irradiation (∼$7.1\,10^9$ erg s$^{-1}$ cm$^{-2}$) make it an excellent target for atmospheric studies via secondary eclipse observations. Using the TRAnsiting Planets and PlanetesImals Small Telescope, we indeed detect its emission in the $z'$-band at better than $\sim 4\sigma$, the measured occultation depth being $603 \pm 130$ ppm. Finally, from a measurement of the Rossiter–McLaughlin effect with the CORALIE spectrograph, we infer a sky-projected spin-orbit angle of $257.^\circ 8^{+5.^\circ 3}_{-5.^\circ 5}$. This result may suggest a significant misalignment between the spin axis of the host star and the orbital plane of the planet. If confirmed, this high misalignment would favour a migration of the planet involving strong dynamical events with a third body.

**Key words:** techniques: photometric – techniques: radial velocities – techniques: spectroscopic – stars: individual: WASP-121 – planetary systems.

## 1 INTRODUCTION

Most of the transiting exoplanets found by ground-based transit surveys (e.g. WASP, Pollacco et al. 2006; HATNet, Bakos et al. 2004) are Jovian-type planets with orbital periods of just a few days, these planets being the easiest to detect for such surveys. The orbital period distribution of these so-called 'hot Jupiters' is not smooth and presents a pile-up around periods of ∼3–4 d (see e.g. Cumming 2010). While the long-period drop-off can be explained by a lower transit probability for these systems combined to a selection effect, the reduced number of planets in orbital periods less than 2 d is definitely real, being seen in both ground- (e.g. WASP; Hellier et al.

★ E-mail: ldelrez@ulg.ac.be
† Fellow of the Swiss National Science Foundation.

2012) and space-based (e.g. *Kepler*; Howard et al. 2012) transit surveys, as well as in radial velocity (RV) surveys (see e.g. Marcy et al. 2004).

Ford & Rasio (2006) suggested that the lower edge of the pile-up is defined not by an orbital period, but rather by a tidal limit, and found that the inner cutoff is actually close to twice the Roche limit ($a_R$).[1] This can be naturally explained if planets were initially scattered into highly eccentric orbits with short pericentre distances from much further out, due to e.g. planet–planet interactions (e.g. Rasio & Ford 1996; Weidenschilling & Marzari 1996; Moorhead & Adams 2005; Chatterjee et al. 2008) and/or Kozai cycles (e.g. Kozai 1962; Lidov 1962; Wu & Murray 2003; Fabrycky & Tremaine 2007), and later circularized via tidal dissipation. On the contrary, they argued that this result is inconsistent with a disc-driven migration scenario (e.g. Goldreich & Tremaine 1980; Lin & Papaloizou 1986; Tanaka, Takeuchi & Ward 2002; Lubow & Ida 2010), as the inner edge of the orbital period distribution should then be right at the Roche limit. The observed distribution of orbital obliquities, with many planets found on misaligned or retrograde orbits (e.g. Triaud et al. 2010), also supports dynamical migration processes involving a third perturbing body, rather than disc migration.

The finding of several hot Jupiters with orbital separations $a$ lower than 2 $a_R$, such as WASP-12 b ($a/a_R \sim 1.09$; Hebb et al. 2009), WASP-19 b ($a/a_R \sim 1.08$; Hebb et al. 2010), WASP-103 b ($a/a_R \sim 1.16$; Gillon et al. 2014), OGLE-TR-56 b ($a/a_R \sim 1.23$; Konacki et al. 2003; Adams et al. 2011), and WTS-2 b ($a/a_R \sim 1.27$; Birkby et al. 2014), challenged the scattering scenario as these planets would have been destroyed or completely ejected from their systems if they had been directly scattered to such short pericentre distances (see e.g. Guillochon, Ramirez-Ruiz & Lin 2011). However, Matsumura, Peale & Rasio (2010) showed that these extreme orbits can still result from the scattering model, assuming first a scattering into an eccentric orbit beyond 2 $a_R$, followed by a slow inward migration and circularization through tidal dissipation inside the planet mainly until reaching $\sim$2 $a_R$, and from then tidal decay through tidal dissipation inside the star only. The speed of the final tidal decay depends on the tidal dissipation efficiency of the star, which is parametrized by $Q'_\star$, the stellar tidal dissipation factor. Despite being an essential parameter in the theory of stellar tides, $Q'_\star$ is still poorly constrained, with estimates based on theoretical and observational studies ranging from $10^5$ to $10^9$ (see e.g. Jackson, Greenberg & Barnes 2008; Ogilvie 2009; Penev, Jackson, Spada & Thom 2012).

Planets in the $a/a_R < 2$ regime are thus key objects to further advance our understanding of how tidal forces influence the orbital evolution of close-in giant planets. Furthermore, these planets being highly irradiated due to their proximity to their host stars, they are also generally favourable targets for atmospheric studies via secondary eclipse observations (see e.g. Gillon et al. 2010; Seager & Deming 2010; Anderson et al. 2013). They thus provide us with a unique opportunity to study the relationship between the observed atmospheric properties of hot Jupiters and their tidal evolution stage. In this paper, we report the discovery of a new hot Jupiter of this rare kind by the WASP survey, WASP-121 b, which orbits a 10.4 $V$-magnitude F-type star at just $\sim$1.15 times its Roche limit.

Section 2 presents the WASP discovery photometry, as well as the follow-up photometric and spectroscopic observations that we used to confirm and characterize the system. In Section 3, we describe the spectroscopic determination of the stellar properties and the derivation of the system parameters through a combined analysis of our photometric and spectroscopic data. The statistical validation of the planet is then described in Section 4. Finally, we discuss our results in Section 5.

[1] I.e. the critical orbital separation inside which a planet would lose mass via Roche lobe overflow.

## 2 OBSERVATIONS

### 2.1 WASP transit detection photometry

The WASP transit survey is operated from two sites with one for each hemisphere: the Observatorio del Roque de los Muchachos in the Canary Islands in the north and the Sutherland Station of the South African Astronomical Observatory (SAAO) in the south. Each facility consists of eight Canon 200 mm f/1.8 focal lenses coupled to e2v 2048×2048 pixels CCDs, which yields a field of view of 450 deg$^2$ for each site with a corresponding pixel scale of 13.7 arcsec pixel$^{-1}$. Observations are done using a broad-band filter with a defined passband from 400 to 700 nm. The exposure time used for the survey is 30 s, and the fields are observed with a typical cadence of 8 min, in a repetitive sequence of seven to eight fields, depending on visibility constraints. Further details of the instruments, survey, and data reduction procedures can be found in Pollacco et al. (2006), while details of the candidate selection process can be found in Collier Cameron et al. (2006) and Collier Cameron et al. (2007).

The host star WASP-121 (1SWASPJ071024.05−390550.5 = 2MASS07102406−3905506, $V = 10.4$, $K = 9.4$) was observed by the WASP-South station (Hellier et al. 2011) from 2011 Oct 28 to 2012 Mar 29, leading to the collection of 9642 photometric measurements. The data were processed with the reduction pipeline described in Pollacco et al. (2006), whose main steps are: standard calibration (bias, dark, and flat-field correction), astrometric calibration, aperture photometry, and extinction and zero-point corrections. The procedures detailed in Collier Cameron et al. (2006), which are based on the Box Least-Squares (Kovács, Zucker & Mazeh 2002) and SysRem (Tamuz, Mazeh & Zucker 2005) detrending algorithms, were then used to search the data for transit signals, leading to the detection of periodic dimmings of about 1.6 per cent with a period of 1.27 d. Fig. 1 presents the WASP photometry folded on the best-fitting transit ephemeris.

The sine-wave fitting method described in Maxted et al. (2011) was used to search for periodic modulation in the WASP photometry of WASP-121 that would be caused by the combination of stellar activity and rotation, but no periodic signal was found above the

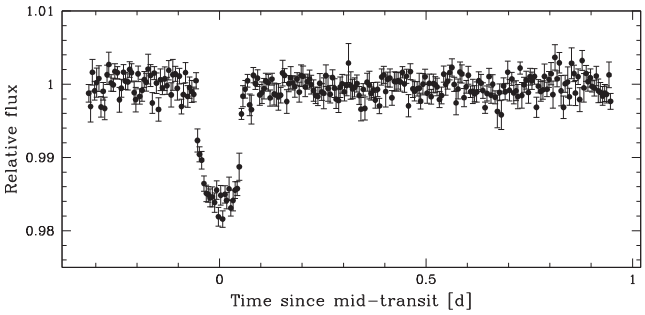


**Figure 1.** WASP photometry for WASP-121 folded on the best-fitting transit ephemeris from the transit search algorithm presented in Collier Cameron et al. (2006), and binned per 0.005 d intervals.

**Table 1.** CORALIE RV measurements for WASP-121. The uncertainties ($\sigma_{RV}$) are the formal errors (i.e. with no added jitter). For each measurement, the table also gives the CCF BS and FWHM, the exposure time ($T_{exp}$), and the seeing. The last two columns indicate whether the measurement was obtained before or after the replacement of the CORALIE optical fibre (see Section 2.2), and in (RM effect) or out of transit. This table is available in its entirety via the CDS.

| HJD −2450 000 | RV (km s$^{-1}$) | $\sigma_{RV}$ (km s$^{-1}$) | BS (km s$^{-1}$) | FWHM (km s$^{-1}$) | $T_{exp}$ (s) | Seeing (arcsec) | Pre-/post-upgrade | In/out of transit |
|---|---|---|---|---|---|---|---|---|
| 6546.907310 | 38.163 52 | 0.017 12 | 0.16642 | 19.622 20 | 1800.798 | 0.40 | Pre | Out |
| 6567.885240 | 38.554 88 | 0.019 96 | −0.27337 | 19.618 06 | 1800.838 | 0.92 | Pre | Out |
| 6577.854124 | 38.544 14 | 0.018 99 | −0.17261 | 19.737 38 | 1800.757 | 0.72 | Pre | Out |
| – | – | – | – | – | – | – | – | – |

mmag amplitude. This analysis was performed over the frequency interval 0–1.5 cycles d$^{-1}$ at 8192 evenly spaced frequencies.

### 2.2 Spectroscopy and RVs

The CORALIE spectrograph (Queloz et al. 2000), mounted on the 1.2 m Euler-Swiss telescope at the ESO La Silla Observatory (Chile), was used to gather 89 spectroscopic measurements of WASP-121 between 2013 Sep 11 and 2015 Jan 12 (we note that the optical fibre feeding the instrument was replaced in 2014 Nov). Among these spectra, 19 were obtained during the transit of 2014 Dec 24 and 18 during the transit of 2015 Jan 12, with the aim of measuring the Rossiter–McLaughlin (RM) effect (McLaughlin 1924; Rossiter 1924). WASP-121 was indeed considered an interesting target for such measurements, as its high projected rotation velocity $v_\star \sin i_\star$ of $13.5 \pm 0.7$ km s$^{-1}$ (see Section 3.1), combined with the observed transit depth, was expected to yield an RM effect with a semi-amplitude $\sim$160 m s$^{-1}$ (in the case of an aligned or anti-aligned orbit).

The spectra, covering the wavelength range from 381 to 681 nm at a resolution of $\sim$55 000, were processed with the CORALIE standard data reduction pipeline (Baranne et al. 1996). RVs were then computed from the spectra by weighted cross-correlation (Pepe et al. 2002), using a numerical G2-spectral template that provides optimal precisions for late-F to early-K dwarfs (Table 1). A preliminary orbital analysis of the RV time series revealed a 1.27 d periodic variation (see the top panel of Fig. 8), in phase with the WASP photometry, and with a semi-amplitude $\sim$180 m s$^{-1}$ compatible with a planetary-mass companion (see Figs 2 a or b). The RM effect was found to have a surprisingly low total amplitude $\sim$80 m s$^{-1}$, suggesting that the planetary orbit may be polar (see Fig. 3). It also appeared that the star exhibits an especially high scatter in its RV residuals: the standard deviation of the best-fitting residuals is 67.1 m s$^{-1}$ for a circular model and 66.0 m s$^{-1}$ for an eccentric model, while the average RV error is 30.7 m s$^{-1}$. We consider further the origin of this high jitter in Section 3.2.

The cross-correlation function (CCF) bisector span (BS; Queloz et al. 2001) and full width at half-maximum (FWHM) values are plotted in Figs 2(c) and (d), respectively. Both present large variations, their standard deviations being 190.2 and 245.9 m s$^{-1}$, respectively, while their average error (calculated as 2.5 times the average RV error; see Santerne et al. 2015) is 76.7 m s$^{-1}$. These variations do not phase with the transit ephemeris, as one might expect if the observed RV signal was originating from a false-positive scenario, such as a blended eclipsing binary (see e.g. Santos et al. 2002); the slope deduced from linear regression of the CCF BS (respectively, FWHM) on the orbital phase is $-0.05 \pm 0.09$ (respectively, $-0.09 \pm 0.11$). However, as the scatter in the BS values is comparable to the semi-amplitude of the RV signal, we were not able to discard blend scenarios based on the traditional BS technique (Queloz et al. 2001). Instead, we performed a detailed blend analysis and used the PASTIS Bayesian software (Díaz et al. 2014; Santerne et al. 2014) to statistically validate the planet, as described in Section 4.

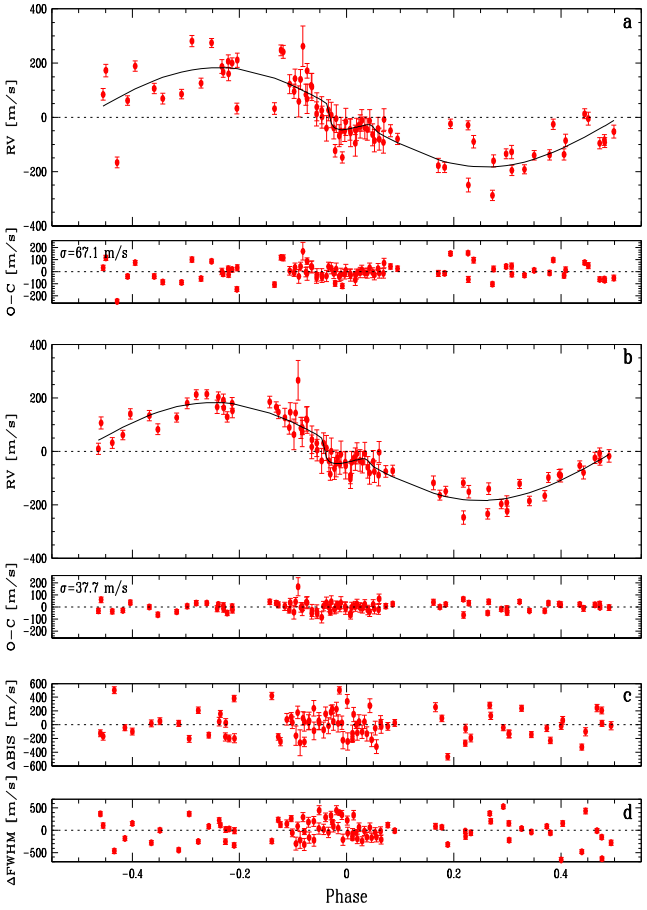


**Figure 2.** (a) CORALIE RVs for WASP-121 phase-folded on the best-fitting transit ephemeris, along with the best-fitting circular model and residuals (jitter is not included in the error bars). (b) Same as the top panel but here first-order polynomial functions of the CCF BS and FWHM were subtracted from the RVs (see Section 3.3). The scatter in the RV residuals is significantly reduced. (c) Change in the CCF BS as a function of orbital phase. (d) Change in the CCF FWHM as a function of orbital phase.

### 2.3 Follow-up eclipse photometry

To refine the system's parameters, high-precision eclipse (transit and occultation) light curves were obtained using the 60 cm TRAPPIST robotic telescope (TRAnsiting Planets and PlanetesImals Small Telescope) and the EulerCam CCD camera that is mounted on the 1.2 m Euler-Swiss telescope, which are both located at ESO La

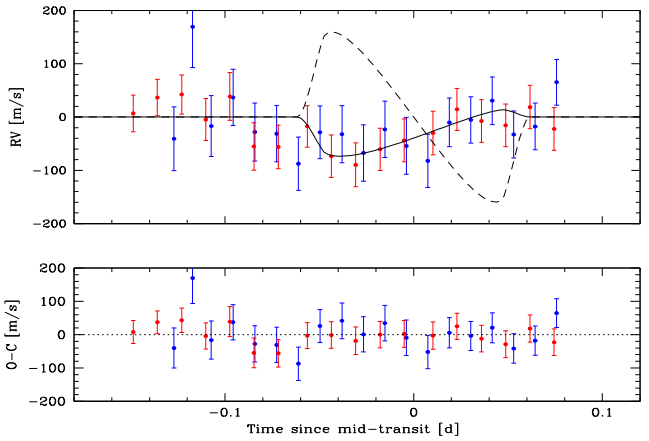


**Figure 3.** Top: zoom on the RM effect observed with CORALIE. The RVs obtained during the transit of 2014 Dec 24 are plotted in blue, while the RVs obtained during the transit of 2015 Jan 12 are plotted in red. The best-fitting circular Keplerian model (orbital motion) has been subtracted for clarity. The superimposed, solid black line is our best-fitting model for the RM effect. The dashed line is the RM effect that would have been observed in the case of an aligned orbit (shown for comparison). Bottom: residuals from our best-fitting model.

Silla Observatory. These follow-up light curves are summarized in Table 2 and presented in Figs 4 and 5. The transits were observed in different filters to search for a potential colour dependence of the transit depth, which might have been indicative of a blend (see Section 4).

#### 2.3.1 *TRAPPIST observations*

TRAPPIST is a 60 cm robotic telescope dedicated to the detection and characterization of transiting exoplanets and to the photometric monitoring of bright comets and other small bodies. It is equipped with a thermoelectrically cooled 2K × 2K CCD, which has a pixel scale of 0.65 arcsec that translates into a 22 arcmin × 22 arcmin field of view. For details of TRAPPIST, see Gillon et al. (2011) and Jehin et al. (2011). TRAPPIST was used to observe four transits of WASP-121 b in a Sloan-$z'$ filter (effective wavelength = 895 ± 1 nm, wavelength range = 816–991 nm) and one transit in a Johnson-$B$ filter (effective wavelength = 440 ± 1 nm, wavelength range = 381–491 nm). As we noticed from a preliminary analysis that WASP-121 b is actually an extremely favourable target for secondary eclipse measurements (we will elaborate on this in Section 5.4), we also observed seven occultation windows in the Sloan-$z'$ filter. During the runs, the positions of the stars on the chip were maintained to within a few pixels thanks to a 'software guiding' system that regularly derives an astrometric solution for the most recently acquired image and sends pointing corrections to the mount if needed. After a standard pre-reduction (bias, dark, and flat-field correction), the stellar fluxes were extracted from the images using the IRAF/DAOPHOT[2] aperture photometry software (Stetson 1987). For each light curve, we tested several sets of reduction parameters and kept the one giving the most precise photometry for the stars of similar brightness as the target. After a careful selection of reference stars, the photometric light curves were finally obtained using differential photometry.

#### 2.3.2 *EulerCam observations*

EulerCam is a 4K × 4K E2V CCD installed at the Cassegrain focus of the 1.2 m Euler-Swiss telescope. The field of view of EulerCam is 15.7 arcmin × 15.7 arcmin, producing a pixel scale of 0.23 arcsec. To keep the stars on the same locations on the detector during the observations, EulerCam employs an 'Absolute Tracking' system that is very similar to the one of TRAPPIST, which matches the point sources in each image with a catalogue, and if needed, adjusts the telescope pointing between exposures to compensate for drifts. EulerCam was used to observe two transits of WASP-121 b in a Gunn-$r'$ filter (effective wavelength = 664 ± 1 nm, wavelength range = 601–725 nm) and two other transits in a Geneva-$B$ filter[3] (effective wavelength = 425 ± 1 nm, wavelength range = 375–475 nm). A slight defocus was applied to the telescope to optimize the observation efficiency and to minimize pixel-to-pixel effects. The reduction procedure used to extract the transit light curves was similar to that performed on TRAPPIST data. Further details of the EulerCam instrument and data reduction procedures can be found in Lendl et al. (2012).

### 2.4 Out-of-eclipse photometric monitoring

To search for potential out-of-eclipse photometric variability that would not have been detected in the WASP photometry (see Section 2.1), we monitored WASP-121 with TRAPPIST for 27 non-consecutive nights between 2014 Oct 25 and 2014 Dec 8. This monitoring consisted in taking every night a short sequence of 10 images in three filters: Johnson-$B$ (effective wavelength = 440 ± 1 nm, wavelength range = 381–491 nm), Johnson-$V$ (effective wavelength = 546.5 ± 1 nm, wavelength range = 486–617 nm), and Sloan-$z'$ (effective wavelength = 895 ± 1 nm, wavelength range = 816–991 nm). The data were reduced as described in Section 2.3.1. The globally normalized differential light curves obtained in each filter are shown in Fig. 6. WASP-121 appears to be very quiet in photometry, the standard deviations of the binned light curves being 1.6 mmag ($B$), 1.3 mmag ($V$), and 1.1 mmag ($z'$).

## 3 ANALYSIS

### 3.1 Spectroscopic analysis

The individual CORALIE spectra were co-added to produce a single spectrum with an average S/N of around 150:1. The analysis was performed using standard pipeline reduction products and the procedures given in Doyle et al. (2013). The derived stellar parameters are listed in Table 4.

The excitation balance of the Fe I lines was used to determine the effective temperature $T_{\rm eff}$ (6460 ± 140 K). The surface gravity log $g_\star$ (4.2 ± 0.2) was determined from the ionization balance of Fe I and Fe II. The Ca I line at 6439 Å and the Na I D lines were also used as log $g_\star$ diagnostics. The iron abundance was determined from equivalent width measurements of several unblended lines and is relative to the solar value obtained by Asplund et al. (2009). A value for microturbulence ($\xi_{\rm t}$ = 1.5 ± 0.1 km s$^{-1}$) was determined from Fe I using the method of Magain (1984). The quoted error estimates

[2] IRAF is distributed by the National Optical Astronomy Observatory, which is operated by the Association of Universities for Research in Astronomy, Inc., under cooperative agreement with the National Science Foundation.

[3] http://obswww.unige.ch/gcpd/ph13.html

**Table 2.** Summary of the follow-up eclipse photometry obtained for WASP-121. For each light curve, this table shows the date of acquisition (UT), the used instrument, the eclipse nature, the filter and exposure time, the number of data points, the selected baseline function, the standard deviation of the best-fitting residuals (unbinned and binned per intervals of 2 min), and the deduced values for $\beta_w$, $\beta_r$ and $CF = \beta_w \times \beta_r$ (see Section 3.3 for details). For the baseline function, $p(\epsilon^N)$ denotes, respectively, a $N$-order polynomial function of time ($\epsilon = t$), airmass ($\epsilon = a$), PSF FWHM ($\epsilon = f$), background ($\epsilon = b$), and $x$ and $y$ positions ($\epsilon = xy$). For the TRAPPIST data, the symbol $o$ denotes an offset fixed at the time of the meridian flip.

| Date (UT) | Instrument | Eclipse nature | Filter | $T_{exp}$ (s) | $N_p$ | Baseline function | $\sigma$ (per cent) | $\sigma_{120s}$ (per cent) | $\beta_w$ | $\beta_r$ | $CF$ |
|---|---|---|---|---|---|---|---|---|---|---|---|
| 2013 Dec 09 | TRAPPIST | Transit | Sloan-$z'$ | 13 | 763 | $p(t^1) + o$ | 0.26 | 0.12 | 1.12 | 1.52 | 1.70 |
| 2013 Dec 25 | TRAPPIST | Occultation | Sloan-$z'$ | 13 | 902 | $p(a^1{+}xy^1) + o$ | 0.37 | 0.17 | 1.44 | 1.07 | 1.54 |
| 2013 Dec 30 | TRAPPIST | Occultation | Sloan-$z'$ | 13 | 653 | $p(t^1{+}xy^1) + o$ | 0.29 | 0.14 | 1.44 | 1.44 | 2.06 |
| 2014 Jan 01 | TRAPPIST | Transit | Sloan-$z'$ | 13 | 765 | $p(t^1{+}xy^1) + o$ | 0.25 | 0.13 | 1.13 | 2.35 | 2.66 |
| 2014 Jan 13 | TRAPPIST | Occultation | Sloan-$z'$ | 13 | 867 | $p(a^1{+}xy^1) + o$ | 0.27 | 0.12 | 1.07 | 1.56 | 1.66 |
| 2014 Jan 20 | EulerCam | Transit | Gunn-$r'$ | 50 | 235 | $p(t^1{+}f^2)$ | 0.10 | 0.07 | 1.38 | 1.28 | 1.76 |
| 2014 Jan 24 | EulerCam | Transit | Gunn-$r'$ | 50 | 195 | $p(t^1{+}f^2{+}xy^1)$ | 0.14 | 0.09 | 2.45 | 1.10 | 2.70 |
| 2014 Jan 31 | TRAPPIST | Occultation | Sloan-$z'$ | 12 | 947 | $p(a^1) + o$ | 0.25 | 0.10 | 1.12 | 1.00 | 1.12 |
| 2014 Feb 05 | TRAPPIST | Occultation | Sloan-$z'$ | 12 | 1033 | $p(t^1{+}xy^1) + o$ | 0.39 | 0.17 | 1.31 | 1.49 | 1.95 |
| 2014 Mar 22 | TRAPPIST | Occultation | Sloan-$z'$ | 12 | 1007 | $p(t^1{+}xy^1) + o$ | 0.38 | 0.16 | 1.17 | 1.18 | 1.38 |
| 2014 Apr 07 | TRAPPIST | Transit | Sloan-$z'$ | 13 | 700 | $p(a^1{+}xy^1)$ | 0.48 | 0.19 | 1.61 | 1.45 | 2.32 |
| 2014 Apr 14 | TRAPPIST | Occultation | Sloan-$z'$ | 11 | 851 | $p(a^1)$ | 0.36 | 0.16 | 1.02 | 1.58 | 1.61 |
| 2014 Nov 08 | TRAPPIST | Transit | Johnson-$B$ | 7 | 966 | $p(t^2{+}b^2{+}xy^1)$ | 0.55 | 0.23 | 1.46 | 1.09 | 1.59 |
| 2014 Dec 01 | EulerCam | Transit | Geneva-$B$ | 90 | 162 | $p(a^1{+}f^4{+}xy^1)$ | 0.11 | 0.11 | 1.51 | 1.05 | 1.59 |
| 2014 Dec 24 | TRAPPIST | Transit | Sloan-$z'$ | 8 | 961 | $p(a^1)$ | 0.29 | 0.12 | 0.91 | 2.07 | 1.87 |
| 2014 Dec 29 | EulerCam | Transit | Geneva-$B$ | 60 | 223 | $p(a^1{+}f^4)$ | 0.08 | 0.06 | 1.15 | 1.19 | 1.36 |

include those given by the uncertainties in $T_{\rm eff}$ and $\log g_\star$, as well as the scatter due to measurement and atomic data uncertainties.

The projected stellar rotation velocity $v_\star \sin i_\star$ was determined by fitting the profiles of several unblended Fe I lines. A macro-turbulent velocity ($v_{\rm mac}$) of $6.0 \pm 0.6$ km s$^{-1}$ was assumed using the asteroseismic-based calibration of Doyle et al. (2014) and an instrumental resolution of 55 000. A best-fitting value of $v_\star \sin i_\star = 13.5 \pm 0.7$ km s$^{-1}$ was obtained.

There is no significant detection of lithium in the spectra, with an abundance upper limit log A(Li)$<$1.0. The lack of any detectable lithium does not provide an age constraint as the star's $T_{\rm eff}$ places it in the lithium gap (Böhm-Vitense 2004). There is also no significant chromospheric emission in the Ca II H and K line cores.

The spectral type (F6V) was estimated from $T_{\rm eff}$ using the table B 1 in Gray (2008) and the Torres, Andersen & Giménez (2010) calibration was used to obtain first stellar mass and radius estimates: $M_\star = 1.37 \pm 0.14$ M$_\odot$ and $R_\star = 1.52 \pm 0.41$ R$_\odot$.

### 3.2 Stellar jitter

As mentioned in Section 2.2, WASP-121 exhibits an especially high scatter in its RV residuals (Fig. 2a), CCF BS (Fig. 2c), and FWHM (Fig. 2d). Fig. 7 compares the RV residuals from our best-fitting circular model (Fig. 2a) to the CCF BS. There is a significant anti-correlation between these two quantities, the correlation coefficient being $-0.68$. Such an anticorrelation is commonly interpreted as being a signature of stellar activity (see e.g. Queloz et al. 2001; Melo et al. 2007), but Santerne et al. (2015) showed that it could also be produced by a blended star with a lower CCF FWHM (and thus slower rotation) than the target star. However, as detailed in Section 4, we were not able to reproduce the observed RVs, CCF BS, and FWHM assuming such a scenario, thus making it likely that the high jitter measured for WASP-121 is due to stellar activity. One might have concerns about the non-detection of this stellar activity in the form of emission in the Ca II H and K line cores (see Section 3.1), out-of-eclipse photometric variability (see Sections 2.1 and 2.4), or spot-crossing events during transits (see Fig. 4). A detailed study of WASP-121's activity being beyond the scope of this paper, we just propose here some potential explanations regarding these non-detections.

First, we note that such a situation is not atypical for an F-type star as it was also encountered for the exoplanet F-type host stars HAT-P-33 (Hartman et al. 2011) and WASP-111 (Anderson et al. 2014), which both present high activity-related RV jitter with no other apparent sign of stellar activity. More precisely, in the case of WASP-111, the scatter in the RV residuals, CCF BS and FWHM dropped from one season to the next, identifying clearly stellar activity as an origin for these.

Secondly, it can be seen from Noyes et al. (1984) that the chromospheric Ca II emission of stars decreases with lowering $B - V$. As WASP-121's $B - V$ is only 0.43, its Ca II emission could simply be too weak to be detected in our low S/N CORALIE spectra.

As for the non-detections of out-of-eclipse variations or spot-crossing events in the photometry, they might be explained, at least to some extent, if the star is plage-dominated, in opposition to spot-dominated (see Dumusque, Boisse & Santos 2014). Both spots and plages are regions of strong magnetic fields that inhibit locally the convection and suppress the convective blueshift (CB) effect (see e.g. Dravins, Lindegren & Nordlund 1981). These regions are thus redshifted compared to the quiet photosphere. Furthermore, as their temperatures differ from the average effective temperature of the star, they have a different flux from that of the average stellar surface. They thus break the flux balance between the blueshifted approaching side and the redshifted receding side of the rotating star (flux effect). Due to both these effects, spots and plages induce RV variations as they pass on the visible stellar disc due to stellar rotation. The CB effect is expected to be similar for spots and plages of the same size. However, plages present a much lower flux ratio with the quiet photosphere compared to spots (see Dumusque et al. 2014 for details), so that they induce a smaller flux effect and a smaller photometric variability.

Fig. 8 shows Lomb–Scargle periodograms (Scargle 1982) of the RV residuals (assuming a circular orbit, second panel from the top), CCF BS (third panel from the top), and FWHM (bottom panel). In

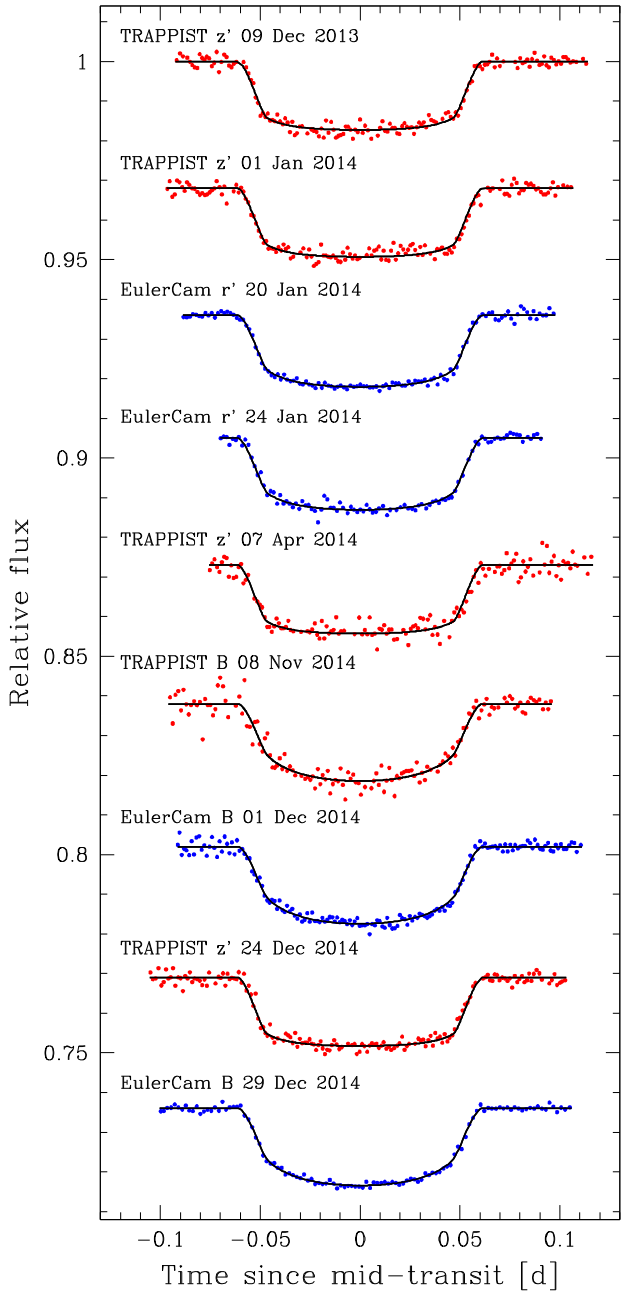


**Figure 4.** Follow-up transit photometry for WASP-121 b. The observations are binned per 2 min and period-folded on the best-fitting transit ephemeris (see Section 3.3). Each light curve has been divided by the respective best-fitting photometric baseline model. For each filter, the superimposed, solid black line is our best-fitting transit model. The light curves are shifted along the *y*-axis for clarity.

each of these periodograms, the highest peaks are found at periods of 0.89, 1.13, and 8.3 d (all with false alarm probabilities $< 0.001$, except for the peak at 1.13 d in the periodogram of the BS). We could assume that one of these three periods, which are each other's daily aliases, is the stellar rotation period $P_{\mathrm{rot},\star}$ (this supposes that the activity-induced RV signal is related to the rotation of the star). A stellar rotation period of 8.3 d does not seem very likely, as the maximal rotation period implied by $v_\star \sin i_\star$ and our final estimate of the stellar radius ($R_\star = 1.458 \pm 0.030$ R$_\odot$, see Section 3.3) is $5.46 \pm 0.32$ d (assuming $\sin i_\star = 1$). Stellar rotation periods of 0.89 and 1.13 d would imply, together with our measured value for $R_\star$, rotation velocities $v_\star$ of $82.9 \pm 1.7$ and $65.3 \pm 1.4$ km s$^{-1}$, respectively, and inclinations $i_\star$ of $9\overset{\circ}{.}4 \pm 0\overset{\circ}{.}6$ and $11\overset{\circ}{.}9 \pm 0\overset{\circ}{.}7$, respectively, where the uncertainties are the quadratic sum of the uncertainties due to each input parameter. In both cases, the star would thus be seen nearly pole-on, i.e. with the rotation axis oriented towards the Earth. If the star is seen nearly pole-on, WASP-121b should then be in a (nearly) polar orbit to produce transits. As mentioned previously, this is actually what our observations of the RM effect suggest (see Sections 3.3 and 5.2), which makes $P_{\mathrm{rot},\star}$ likely to be 0.89 or 1.13 d. We note that for the 1-Gyr-old cluster NGC6811 observed with *Kepler* by Meibom et al. (2013), the stars with $B - V = 0.43$ (such as WASP-121) have ∼1-d rotation periods (see their fig. 1b). As the age of WASP-121 obtained by stellar evolution modelling is $1.5 \pm 1.0$ Gyr (see Section 3.4), a ∼1-d rotation period would thus be consistent with their values.

We used the SOAP 2.0 code of Dumusque et al. (2014) to assess the type of active region (spot or plage) and corresponding surface coverage that would be needed to explain the RV jitter observed for WASP-121 if it is seen nearly pole-on. The code takes as main inputs $T_{\mathrm{eff}}$ ($6460 \pm 140$ K), $R_\star$ ($1.458 \pm 0.030$ R$_\odot$), $P_{\mathrm{rot},\star}$ (∼1 d), and $i_\star$ (∼10$\overset{\circ}{.}$6). If we assume an active region consisting of a spot and an upper limit of 1 mmag (see Section 2.1) for the photometric variability induced by this active region (also returned by the code), the maximal RV peak-to-peak amplitude is obtained for a ∼1.2 per cent[4] spot located at a latitude of ∼80° and is of the order of 90 m s$^{-1}$. This is significantly lower than the ∼300 m s$^{-1}$ amplitude of our RV residuals. Conversely, such an RV amplitude can for example be reproduced if the active region consists of a ∼8 per cent[5] bright plage at a latitude of ∼50° (the corresponding photometric variability having an amplitude of ∼0.14 mmag). The high activity-related RV jitter observed for WASP-121 despite the lack of photometric variability could thus be explained if the star is dominated by plages. We note that a plage-dominated activity was also invoked to account for the RV jitter observed for another active F6V exoplanet host star: $\tau$ Bootis A (see Borsa et al. 2015).

### 3.3 Global modelling of the data

To determine the system parameters, we performed a combined analysis of the follow-up eclipse photometry and the RV data, using for this purpose the adaptive Markov Chain Monte Carlo (MCMC) code described in Gillon et al. (2012) and references therein. To model the photometry, we used the eclipse model of Mandel & Agol (2002) multiplied by a different baseline model for each light curve. These baseline models aim to represent astrophysical, instrumental, or environmental effects, which are able to produce photometric variations and can, therefore, affect the photometric light curves. They can be made up of different first- to fourth-order polynomials with respect to time or other variables, such as airmass, point spread function (PSF) FWHM, background, or stellar position on the detector. To find the optimal baseline function for each light curve, i.e. the model minimizing the number of parameters and the level of noise in the best-fitting residuals, the Bayes factor, as estimated from the Bayesian Information Criterion

[4] This size is defined as the fraction of the surface of the visible hemisphere covered by the active region.

[5] A surface coverage of ∼8 per cent is realistic, as Andretta & Giampapa (1995) estimate that plages can cover more than 20 per cent of the surface of active Sun-like (F-early K) stars.

(BIC; Schwarz 1978), was used. The best photometric baseline functions are listed in Table 2. For eight TRAPPIST light curves (see Table 2), a normalization offset was also part of the baseline model to represent the effect of the meridian flip; that is, the 180° rotation that the German equatorial mount telescope has to undergo when the meridian is reached. This movement results in different positions of the stellar images on the detector before and after the flip, and the normalization offset allows us to take into account a possible consecutive jump in the differential photometry at the time of the flip.

On their side, the RVs were modelled using a classical Keplerian model (e.g. Murray & Correia 2010) added to a baseline model for the stellar and instrumental variability. For the RVs obtained during a transit, the RM effect was modelled using the formulation of Giménez (2006). The RVs were partitioned into four data sets, each with a different baseline model: the RVs obtained before the replacement of the CORALIE optical fibre (37 RVs, data set #1), those obtained after (15 RVs, data set #2), the first RM sequence (19 RVs, data set #3), and the second one (18 RVs, data set #4). For all data sets, the minimal baseline model was a scalar $V_\gamma$ representing the systemic velocity of the star. For data sets #1 and #2, first-order polynomial functions of the CCF BS and FWHM were also part of the baseline models. This choice of baselines allowed us to reduce the scatter in the global RV residuals from 67.1 to 37.7 m s$^{-1}$ (see Figs 2 a and b) and was thus strongly favoured by the BIC. These additional baseline terms were not necessary for the data sets #3 and #4 (RM sequences). Including linear correlations with the CCF parameters in the RV model to account for activity-related RV variations is a technique that has been previously used by other investigators (see e.g. Hartman et al. 2011; Jenkins & Tuomi 2014; Tuomi et al. 2014).

The basic jump parameters in our MCMC analyses, i.e. the parameters that are randomly perturbed at each step of the MCMC, were: the planet/star area ratio $\mathrm{d}F = (R_\mathrm{p}/R_\star)^2$; the occultation depth in the $z'$-band $\mathrm{d}F_{\mathrm{occ},\,z'}$; the transit impact parameter in the case of a circular orbit $b' = a\cos i_\mathrm{p}/R_\star$, where $a$ is the orbital semimajor axis and $i_\mathrm{p}$ is the orbital inclination; the transit width (from first to fourth contact) $W$; the time of mid-transit $T_0$; the orbital period $P$; the stellar effective temperature $T_\mathrm{eff}$; the stellar metallicity [Fe/H]; the parameter $K_2 = K\sqrt{1-e^2}\ P^{1/3}$, where $K$ is the RV orbital semi-amplitude and $e$ is the orbital eccentricity; the two parameters $\sqrt{e}\cos\omega$ and $\sqrt{e}\sin\omega$, where $\omega$ is the argument of the periastron; and the two parameters $\sqrt{v_\star \sin i_\star}\cos\beta$ and $\sqrt{v_\star \sin i_\star}\sin\beta$, where $v_\star \sin i_\star$ is the projected rotational velocity of the star and $\beta$ is the sky-projected angle between the stellar spin axis and the planet's orbital axis. The reasons to use $\sqrt{e}\cos\omega$ and $\sqrt{e}\sin\omega$ as jump parameters instead of the more traditional $e\cos\omega$ and $e\sin\omega$ are detailed in Triaud et al. (2011). The results obtained from the spectroscopic analysis (see Section 3.1) were used to impose normal prior distributions on $T_\mathrm{eff}$, [Fe/H], and $v_\star \sin i_\star$, with expectations and standard deviations corresponding to the quoted measurements and errors, respectively. Uniform prior distributions were assumed for the other parameters. The photometric and RV baseline model parameters were not actual jump parameters; they were determined by least-square minimization from the residuals at each step of the MCMC.

The effect of stellar limb-darkening (LD) on our transit light curves was accounted for using a quadratic LD law, where the quadratic coefficients $u_1$ and $u_2$ were allowed to float in our MCMC analysis. However, we did not use these coefficients themselves as jump parameters but their combinations, $c_1 = 2 \times u_1 + u_2$ and $c_2 = u_1 - 2 \times u_2$, to minimize the correlation of the obtained uncertainties as introduced by Holman et al. (2006). To obtain an LD solution consistent with theory, we used normal prior distributions for $u_1$ and $u_2$ based on theoretical values and $1\sigma$ errors interpolated in the tables by Claret & Bloemen (2011). These prior distributions are presented in Table 3.

A preliminary analysis was performed to determine the correction factors ($CF$) for our photometric errors, as described in Gillon et al. (2012). For each light curve, $CF$ is the product of two contributions, $\beta_w$ and $\beta_r$. On one side, $\beta_w$ represents the underestimation or overestimation of the white noise of each measurement. It is computed as the ratio between the standard deviation of the residuals and the mean photometric error. On the other side, $\beta_r$ allows us to take into account the correlated noise present in the light curve (i.e. the inability of our model to perfectly fit the data). It is calculated from the standard deviations of the binned and unbinned residuals for different binning intervals ranging from 5 to 120 min with the largest value being kept as $\beta_r$. The standard deviation of the best-fitting residuals (unbinned and binned per intervals of 2 min) and the deduced values for $\beta_w$, $\beta_r$ and $CF = \beta_w \times \beta_r$ for each light curve are presented in Table 2. This preliminary analysis also allowed us to compute the jitter values that were added quadratically to the RV errors of each RV data set to equal their mean values to the standard deviations of the best-fits residuals, and thus achieve reduced $\chi^2$ values of unity. These jitter values were 27.9, 22.3, 16.9 m s$^{-1}$, and zero for the data sets #1, #2, #3, and #4, respectively.

A second analysis with the updated photometric and RV errors was then performed to determine the stellar density $\rho_\star$, which can be derived from the Kepler's third law and the jump parameters $(R_\mathrm{p}/R_\star)^2$, $b'$, $W$, $P$, $\sqrt{e}\cos\omega$ and $\sqrt{e}\sin\omega$ (see e.g. Seager & Mallén-Ornelas 2003; Winn 2010). This analysis consisted of two Markov chains of $10^5$ steps, whose convergence was checked using the statistical test of Gelman & Rubin (1992). The first 20 per cent of each chain was considered as its burn-in phase and discarded. The resulting stellar density was used as input of a stellar evolution modelling, together with the effective temperature and metallicity derived from spectroscopy, with the aim to estimate the stellar mass $M_\star$ and the age of the system. This stellar evolution modelling is described in detail in Section 3.4.

Two final analyses were then performed: one assuming a circular orbit ($e = 0$) and one with a free eccentricity. Each analysis consisted of two Markov chains of $10^5$ steps, whose convergence was again checked with the Gelman & Rubin test (Gelman & Rubin 1992). As previously, the first 20 per cent of each chain was considered as its burn-in phase and discarded. At each step of the Markov chains, $\rho_\star$ was computed as described above and a value for $M_\star$ was drawn within a normal distribution having as expectation and standard deviation the value and error obtained from the stellar evolution modelling. The stellar radius $R_\star$ was derived from $M_\star$ and $\rho_\star$, and the other physical parameters of the system were then deduced from the jump parameters and stellar mass and radius. It appeared that the circular orbit was strongly favoured by the Bayes factor ($\sim$5000 in its favour) compared to the eccentric orbit. As there was no evidence for a significant eccentricity ($e < 0.07$ at $3\sigma$), we thus adopted the circular orbit as our nominal solution. The corresponding derived parameters are presented in Table 4, while the best-fitting models are shown in Fig. 2(b) (RVs), 3 (zoom on the RM effect), 4 (transit photometry), and 5 (occultation photometry).

A complementary analysis was finally performed to assess the chromaticity of the transit. In this analysis, transit depth differences between the different filters were added as jump parameters. The deduced transit depths are also presented in Table 4. They are consistent with each other.

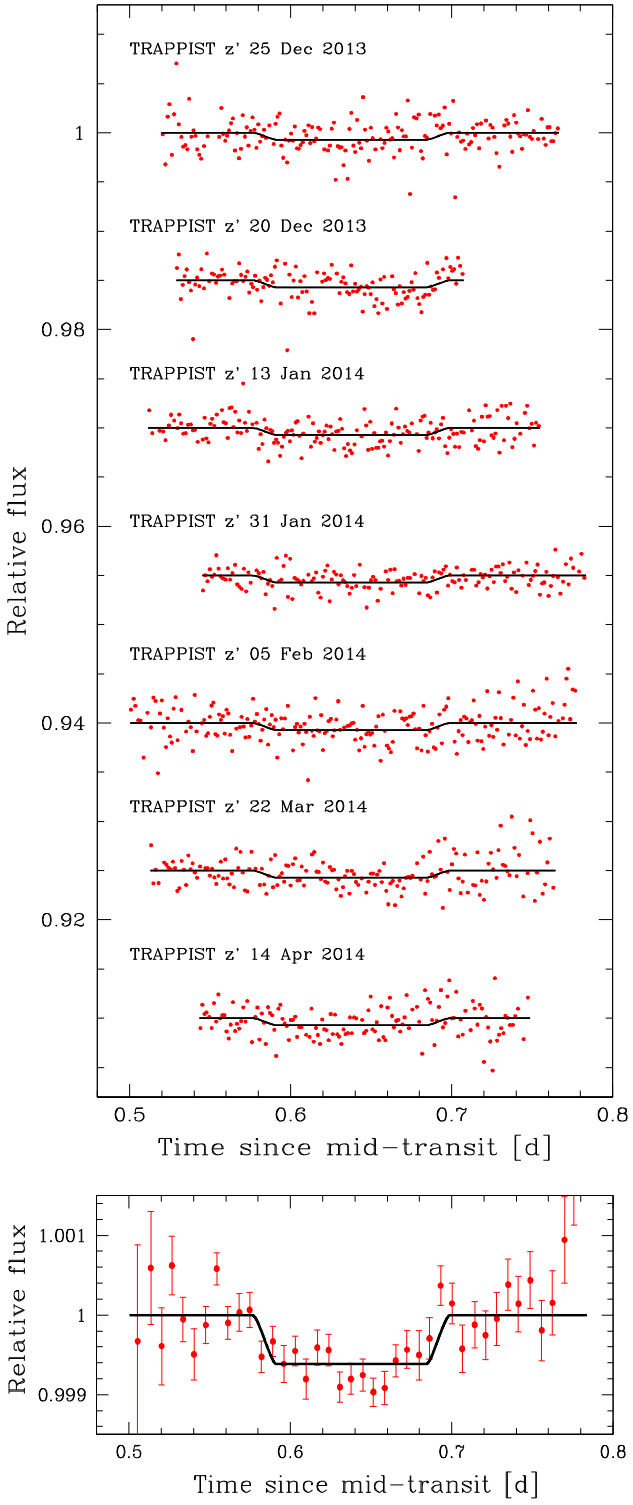


**Figure 5.** Top: individual follow-up occultation light curves for WASP-121 b. The observations are binned per 2 min and period-folded on the best-fitting transit ephemeris (see Section 3.3). Each light curve has been divided by the respective best-fitting photometric baseline model. For each light curve, the superimposed, solid black line is our best-fitting occultation model. The light curves are shifted along the *y*-axis for clarity. Bottom: combined follow-up occultation photometry for WASP-121 b (bin width = 10 min).

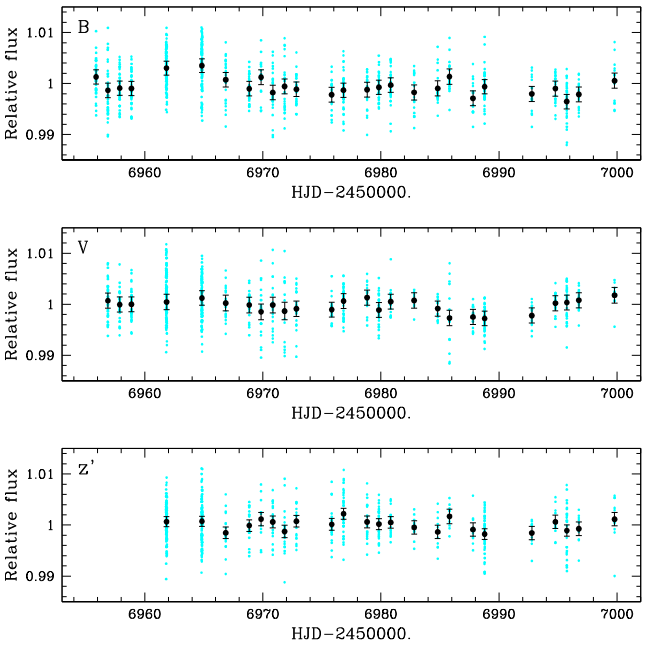


**Figure 6.** Out-of-eclipse photometric monitoring: globally normalized TRAPPIST differential photometry obtained for WASP-121 in Johnson-*B* (top), Johnson-*V* (middle), and Sloan-$z'$ (bottom) filters, unbinned ( cyan) and binned by day (black).

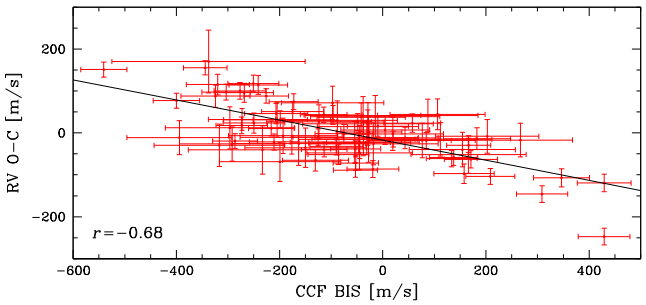


**Figure 7.** RV residuals from the best-fitting circular orbital model versus CCF BS. The two quantities are clearly anticorrelated. A linear fit to the data is overplotted and the correlation coefficient ($r$) is given.

### 3.4 Stellar evolution modelling

As introduced in Section 3.3, we performed for the host star a stellar evolution modelling based on the CLES code (Scuflaire et al. 2008), in order to estimate the stellar mass and the age of the system. We used as inputs the stellar density deduced from the transit light curves, and the effective temperature and metallicity derived from spectroscopy (see Table 4). We considered that [Fe/H] represents the global metallicity with respect to the Sun i.e. $[\mathrm{Fe/H}] = [\log(\mathrm{Z/X})_* - \log(\mathrm{Z/X})_\odot]$, with $(\mathrm{Z/X})_\odot = 0.0181$ (Asplund et al. 2009). The parameter of the mixing-length theory (MLT) of convection was kept fixed to the solar calibration ($\alpha_{\mathrm{MLT}} = 1.8$), and the possible convective core extra-mixing (due to overshooting, rotationally induced mixing, etc.) and microscopic diffusion (gravitational settling) of elements were included.

We obtained a stellar mass of $1.355 \pm 0.080\ \mathrm{M}_\odot$ and an age of $1.5 \pm 1.0$ Gyr. These $1\sigma$ uncertainties were obtained by considering the respective $1\sigma$ range for the effective temperature, metallicity and stellar density, but also by varying the internal stellar physics. We computed, since the helium atmospheric abundance cannot be

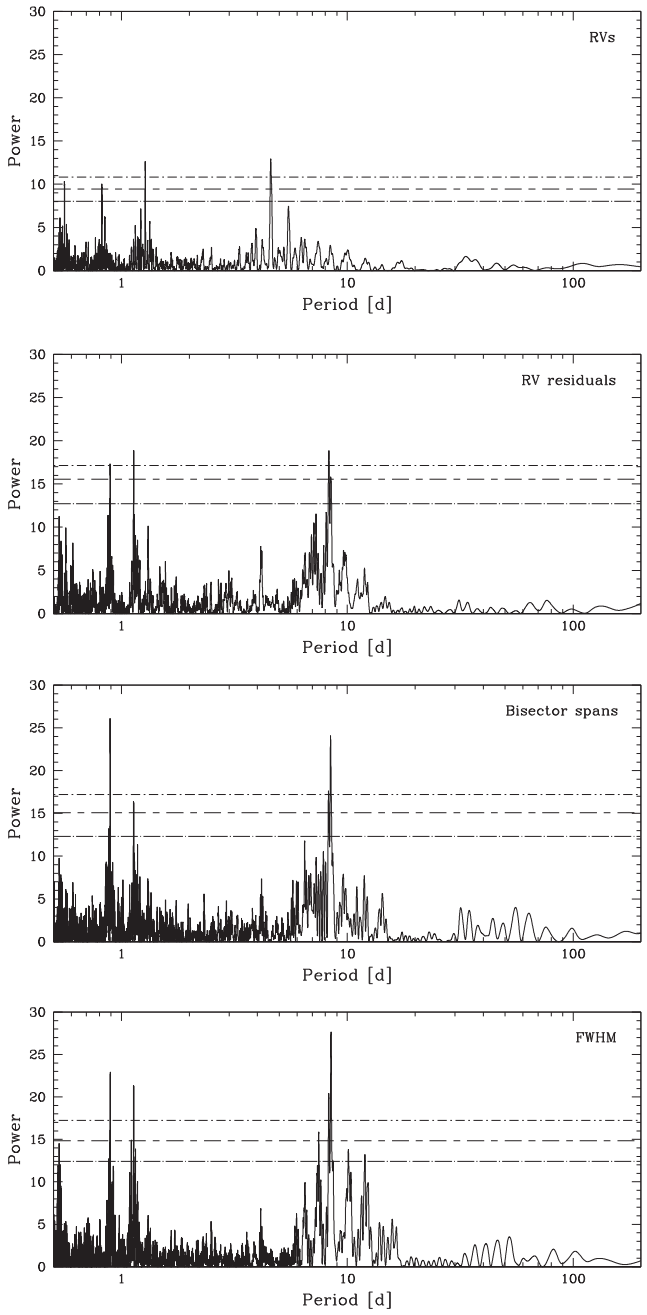


**Figure 8.** From top to bottom: Lomb–Scargle periodograms of the RVs, RV residuals (assuming a circular orbit), CCF BS, and FWHM. Horizontal lines indicate false alarm probability levels of 0.001, 0.01, and 0.1 (from top to bottom).

**Table 3.** Expectations and standard deviations of the normal distributions used as prior distributions for the quadratic LD coefficients $u_1$ and $u_2$ in our MCMC analysis.

| Filter | $u_1$ | $u_2$ |
|---|---|---|
| Sloan-$z'$ | $0.171 \pm 0.014$ | $0.306 \pm 0.006$ |
| Gunn-$r'$ | $0.295 \pm 0.015$ | $0.325 \pm 0.006$ |
| Johnson- and Geneva-$B$ | $0.510 \pm 0.027$ | $0.260 \pm 0.019$ |

directly measured from spectroscopy, evolutionary tracks with two initial helium abundances: the solar value ($Y_{\odot,0} = 0.27$), and a value labelled $Y_G$ that increases with $Z$ (as expected if the local medium follows the general trend observed for the chemical evolution of galaxies; Izotov & Thuan 2010). We also investigated the effects of the possible convective core extramixing, by varying it between 0 and 0.3 (Noels & Montalbán 2013).

Evolutionary tracks are presented on Fig. 9 for several stellar masses and metallicities. Obtaining an accurate stellar mass from evolution modelling primarily needs accurate spectroscopic estimates for the effective temperature but also, very importantly, for the metallicity. Metallicity is a parameter that strongly determines the location of the evolutionary tracks in an Hertzsprung-Russell diagram (compare in Fig. 9 the solid and dashed tracks for identical stellar masses, but with different metallicities). The stellar mass obtained from stellar evolution modelling ($1.355 \pm 0.085$ $M_\odot$) is in excellent agreement with the first estimate derived from the Torres et al. (2010) calibration in Section 3.1. The inferred stellar age of $1.5 \pm 1.0$ Gyr places WASP-121 on the main sequence. The total lifetime on the main sequence (H-core burning) of WASP-121 is 4.3 Gyr for a moderate extramixing $\alpha_{\rm em} = 0.2$, and is reduced to 3.3 Gyr without considering any extramixing process in the core.

## 4 PASTIS VALIDATION

Astrophysical false-positive scenarios such as eclipsing binaries might mimic both the transit and RV signal of a planet (Torres et al. 2005). In some particular configurations, even the RM effect might be mimicked (Santerne et al. 2015). In this case, the line bisector and the FWHM present a large variation. Moreover, we were able to detect from the ground in the $z'$ band a relatively deep secondary eclipse. Both arguments prevent to secure the planetary nature of WASP-121 b without a more careful investigation. We can imagine five scenarios which can reasonably produce the observed data: (1) a planet transiting the target star, (2) a planet transiting a chance-aligned background star, (3) a chance-aligned background eclipsing binary, (4) a planet transiting a physical companion to the target star, and (5) a star eclipsing a physical companion to the target star (i.e. a triple system). The scenarios 2–5 can be split in two categories and discussed separately; the background or physical companion sources of false positive.

### 4.1 A background source

A background source of false positive can mimic the transit data of a planet within a range of magnitude $\Delta m$ defined as (Morton & Johnson 2011)

$$\Delta m = 2.5 \log_{10} \left( \frac{\delta_{\rm tr}}{\delta_{\rm bg}} \right), \quad (1)$$

where $\delta_{\rm tr}$ and $\delta_{\rm bg}$ are the depth of the transit, as measured in the light curve, and the depth of the background eclipse, respectively. Assuming a maximum eclipse depth of 50 per cent for the background star, we find that the maximum magnitude range is of 3.78. Note that a 50 per cent depth eclipsing binary should also produce a secondary eclipse with a similar depth, which is clearly excluded in the case of WASP-121. Therefore, this magnitude range is overestimated, which will also overestimate the probability of a background star as the host of the observed signal. The star is of magnitude 10.44 in the $V$ band, hence false positive can probe stars as faint as magnitude 14.22 in the same bandpass.

**Table 4.** System parameters for WASP-121. The values given for the parameters derived from our MCMC analysis are medians and $1\sigma$ limits of the marginalized posterior probability distributions.

| | | | |
|---|---|---|---|
| *General information* | | | |
| RA (J2000) | $07^{h}\ 10^{m}\ 24\overset{s}{.}06$ | $V$-magnitude | 10.44 |
| Dec. (J2000) | $-39^{\circ}\ 05'\ 50\overset{''}{.}55$ | $K$-magnitude | 9.37 |
| Distance [pc][a] | $270 \pm 90$ | | |
| *Stellar parameters from spectroscopic analysis (Section 3.1)* | | | |
| Spectral type | F6V | Microturbulence $\xi_t$ [km s$^{-1}$] | $1.5 \pm 0.1$ |
| Effective temperature $T_{\rm eff}$ [K] | $6460 \pm 140$ | Macroturbulence $v_{\rm mac}$ [km s$^{-1}$] | $6.0 \pm 0.6$ |
| Surface gravity log $g_\star$ [cgs] | $4.2 \pm 0.2$ | Proj. rot. velocity $v_\star \sin i_\star$ [km s$^{-1}$] | $13.5 \pm 0.7$ |
| Metallicity [Fe/H] [dex] | $0.13 \pm 0.09$ | Lithium abundance log A(Li) [dex] | $< 1.0$ |
| *Parameters from MCMC analysis (Section 3.3)* | | | |
| **Jump parameters** | | | |
| Planet/star area ratio $dF = (R_p/R_\star)^2$ [ per cent] | $1.551 \pm 0.012$ | Effective temperature $T_{\rm eff}$ [K][b] | $6459 \pm 140$ |
| Occultation depth $dF_{{\rm occ},\,z'}$ [ppm] | $603 \pm 130$ | Metallicity [Fe/H] [dex][b] | $0.13 \pm 0.09$ |
| $b' = a\cos i_p/R_\star$ [$R_\star$] | $0.160^{+0.040}_{-0.042}$ | $c_{1,z'} = 2\,u_{1,z'} + u_{2,z'}$ | $0.637^{+0.026}_{-0.025}$ |
| Transit width $W$ [d] | $0.1203 \pm 0.0003$ | $c_{2,z'} = u_{1,z'} - 2\,u_{2,z'}$ | $-0.445 \pm 0.018$ |
| $T_0 - 2450\,000$ [HJD$_{\rm TDB}$] | $6635.708\,32^{+0.00011}_{-0.00010}$ | $c_{1,r'} = 2\,u_{1,r'} + u_{2,r'}$ | $0.904^{+0.027}_{-0.026}$ |
| Orbital period $P$ [d] | $1.274\,9255^{+0.000\,00020}_{-0.000\,00025}$ | $c_{2,r'} = u_{1,r'} - 2\,u_{2,r'}$ | $-0.361^{+0.020}_{-0.018}$ |
| RV $K_2$ [m s$^{-1}$ d$^{1/3}$] | $196.4^{+6.8}_{-6.9}$ | $c_{1,B} = 2\,u_{1,B} + u_{2,B}$ | $1.269^{+0.032}_{-0.031}$ |
| $\sqrt{e}\cos\omega$ | 0 (fixed) | $c_{2,B} = u_{1,B} - 2\,u_{2,B}$ | $-0.012^{+0.043}_{-0.045}$ |
| $\sqrt{e}\sin\omega$ | 0 (fixed) | | |
| $\sqrt{v_\star \sin i_\star}\cos\beta$ | $-0.78 \pm 0.34$ | | |
| $\sqrt{v_\star \sin i_\star}\sin\beta$ | $-3.59^{+0.13}_{-0.11}$ | | |
| **Deduced stellar parameters** | | | |
| Mean density $\rho_\star$ [$\rho_\odot$] | $0.437^{+0.008}_{-0.009}$ | LD coefficient $u_{1,z'}$ | $0.166 \pm 0.013$ |
| Surface gravity log $g_\star$ [cgs] | $4.242^{+0.011}_{-0.012}$ | LD coefficient $u_{2,z'}$ | $0.305 \pm 0.008$ |
| Mass $M_\star$ [M$_\odot$][c] | $1.353^{+0.080}_{-0.079}$ | LD coefficient $u_{1,r'}$ | $0.290 \pm 0.014$ |
| Radius $R_\star$ [R$_\odot$] | $1.458 \pm 0.030$ | LD coefficient $u_{2,r'}$ | $0.325 \pm 0.007$ |
| Luminosity $L_\star$ [$L_\odot$] | $3.3 \pm 0.3$ | LD coefficient $u_{1,B}$ | $0.505 \pm 0.018$ |
| Proj. rot. velocity $v_\star \sin i_\star$ [km s$^{-1}$][b] | $13.56^{+0.69}_{-0.68}$ | LD coefficient $u_{2,B}$ | $0.259^{+0.020}_{-0.019}$ |
| Mean systemic velocity $V_\gamma$ [km s$^{-1}$] | $38.350 \pm 0.021$ | | |
| **Deduced planet parameters** | | | |
| RV $K$ [m s$^{-1}$] | $181.1^{+6.3}_{-6.4}$ | Mean density $\rho_p$ [$\rho_{\rm Jup}$] | $0.201 \pm 0.010$ |
| Planet/star radius ratio $R_p/R_\star$ | $0.124\,54^{+0.000\,47}_{-0.000\,48}$ | Surface gravity log $g_p$ [cgs] | $2.973 \pm 0.017$ |
| $T_{\rm occ} - 2450\,000$ [HJD$_{\rm TDB}$] | $6636.345\,78^{+0.000\,11}_{-0.000\,10}$ | Mass $M_p$ [$M_{\rm Jup}$] | $1.183^{+0.064}_{-0.062}$ |
| Scaled semimajor axis $a/R_\star$ | $3.754^{+0.023}_{-0.028}$ | Radius $R_p$ [$R_{\rm Jup}$] | $1.807 \pm 0.039$ |
| Orbital semimajor axis $a$ [au] | $0.025\,44^{+0.000\,49}_{-0.000\,50}$ | Roche limit $a_R$ [au][d] | $0.022\,05 \pm 0.000\,66$ |
| Orbital inclination $i_p$ [deg] | $87.6 \pm 0.6$ | $a/a_R$ | $1.153 \pm 0.019$ |
| Orbital eccentricity $e$ | 0 (fixed) | Equilibrium temperature $T_{\rm eq}$ [K][e] | $2358 \pm 52$ |
| Argument of periastron $\omega$ [deg] | – | Irradiation [erg s$^{-1}$ cm$^{-2}$] | $7.1^{+1.3}_{-1.1}\ 10^9$ |
| Sky-projected orbital obliquity $\beta$ [deg] | $257.8^{+5.3}_{-5.5}$ | | |
| **Transit depths in the different bands** | | | |
| Planet/star area ratio $dF_{z'}$ [ per cent] | $1.547 \pm 0.013$ | Planet/star area ratio $dF_B$ [ per cent] | $1.551 \pm 0.014$ |
| Planet/star area ratio $dF_{r'}$ [ per cent] | $1.553 \pm 0.013$ | | |
| *Planet parameters corrected for asphericity (Section 5.1)* | | | |
| Radius $R_p$ [$R_{\rm Jup}$] | $1.865 \pm 0.044$ | Mean density $\rho_p$ [$\rho_{\rm Jup}$] | $0.183 \pm 0.016$ |

[a] From $V$ mag and estimated absolute magnitude.
[b] Using as priors the values derived from the spectroscopic analysis.
[c] Using as prior the value obtained from stellar evolution modelling.
[d] Using $a_R = 2.46\,R_p(M_\star/M_p)^{1/3}$ (Chandrasekhar 1987).
[e] Assuming a null Bond albedo and isotropic reradiation (reradiation factor $f = 1/4$; López-Morales & Seager 2007).

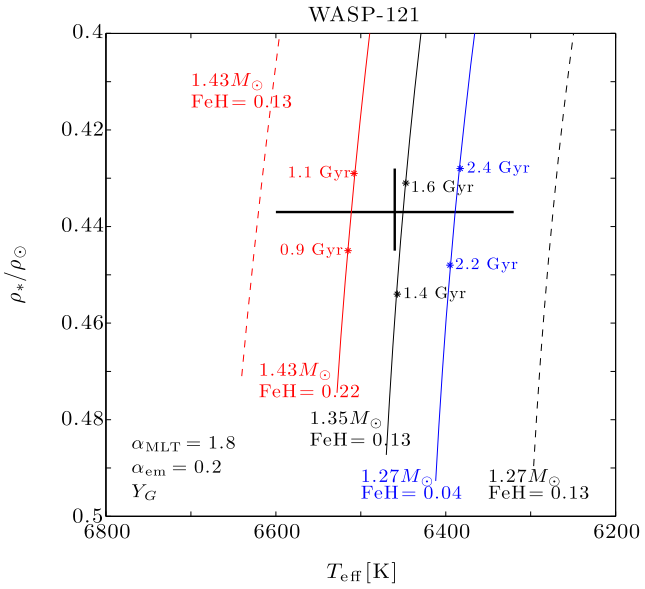


**Figure 9.** Evolutionary tracks in a $T_{\rm eff}$–$\rho_\star/\rho_\odot$ HR diagram for WASP-121, for different masses and metallicities, within (solid lines) and without (dashed lines) the $1\sigma$ box $T_{\rm eff}$–$\rho_\star/\rho_\odot$. Some stellar ages are also indicated.

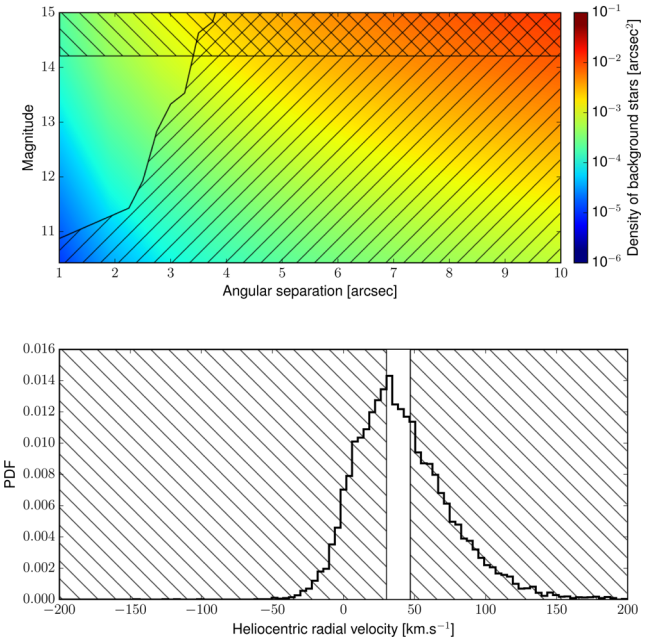


**Figure 10.** Upper panel: map of the density of background stars chance-aligned with WASP-121, integrated within an angular separation of up to 10 arcsec, as function of the *V*-band magnitude. The positive-slope hatched region displays all the stars that would have been significantly detected in the TRAPPIST data. The negative-slope hatched region displays the stars that are too faint to reproduce the observed transit depth of WASP-121. Lower panel: distribution of heliocentric RV of stars within 10° from WASP-121 as observed by the RAVE experiment. The hatched regions show the velocity of background stars that should be spectroscopically resolved with WASP-121 and thus should produce a RV variation in antiphase with the transit ephemeris, or no significant variation (Santerne et al. 2015).

To compute the probability of having a background star chance-aligned with WASP-121, we took the APASS (Henden et al. 2015) DR8 *V* magnitude of all stars within 1° from WASP-121. The magnitude limit of this catalogue is between magnitude 16 and 17, which is about 2 mag above the maximum magnitude of the background star. We therefore assume that this catalogue is complete in the range of magnitude we are considering here. We did not detect in the TRAPPIST data any background source that could host the transit. Thus, in this scenario, the background source should be blended within the TRAPPIST PSF. In Fig. 10, we display the sensitivity curve of the TRAPPIST PSF. This curve was obtained by injecting artificial stars in good-seeing TRAPPIST images at various separations and with a range of magnitude, and then attempting to detect them with IRAF/DAOPHOT. Any star brighter than magnitude 14 and separated from WASP-121 by more than 3.5 arcsec should have been detected. Using these constraints and assuming that the stars are randomly distributed around the target star, we find that the probability for WASP-121 to be chance-aligned with a background star brighter than magnitude 14.22 is at the level of maximum $8.10^{-4}$. If we account for the probability that this hypothetical background star host a binary (∼50 per cent; Raghavan et al. 2010) or a planet (∼50 per cent; Mayor et al. 2011) and the eclipse or transit probability at 1.3 d (∼25 per cent), we end with a a priori probability that the transit signal is hosted by a background star lower than $\sim 1.10^{-4}$.

A significant RV variation has been detected in phase with the transit ephemeris and no other component has been significantly detected in the CORALIE CCFs with a flux ratio greater than 0.7 per cent (i.e. 5.4 mag). Therefore, to mimic both the photometric and RV data of WASP-121, the background source should be chance-aligned along the line of sight and in the RV space. To produce a RV in phase with the transit ephemeris, the background star should have a systemic velocity within the width of the line profile of WASP-121 (Santerne et al. 2015), i.e. the two stars should be spectroscopically unresolved. Given the systemic velocity of WASP-121 ($\gamma \sim 38.3$ km s$^{-1}$) and the width of its line profile observed by CORALIE ($\sigma_{\rm CCF} = {\rm FWHM}/2\sqrt{2\ln(2)} \approx 8.2$ km s$^{-1}$), the background star should thus have a systemic RV in the range [30.1; 46.5] km s$^{-1}$. We then compared this range of RV with the distribution of stars in the vicinity of WASP-121 from the RAVE data base (Kordopatis et al. 2013). The offset between the CORALIE zero-point and the RAVE reference is expected to be less than a few hundreds of m s$^{-1}$. We took all the stars observed by this spectroscopic survey within 10° of WASP-121 for which we display their RV distribution in Fig. 10. Only 20 per cent of the stars in the vicinity of WASP-121 should be spectroscopically unresolved. Assuming that the position of a star in a place of the sky is independent from its RV, we find that the a priori probability that the signal observed in WASP-121 is caused by a background source is, at most, at the level of 20 ppm. We can therefore exclude all background false-positive scenarios as the source of the detected signal.

### 4.2 A physical companion

Apart from the planet scenario, the most likely scenario to reproduce both the photometric and spectroscopic data is a system physically bound with the target star. In such configuration, the various stellar components could be easily blended in both the plane of the sky and the RV space. Then, the transit could be mimicked either by an eclipsing star or a transiting substellar object.

To estimate the probability that WASP-121 is either a planet transiting the target, a physical companion (planet in binary) or a

triple system, we used the PASTIS software (Díaz et al. 2014; Santerne et al. 2014; Santerne et al. 2015) to model the 11 230 photometric measurements obtained by TRAPPIST and EulerCam in different filters. The light curve was modelled using the EBOP code (Nelson & Davis 1972; Etzel 1981; Popper & Etzel 1981) extracted from the JKTEBOP package (Southworth 2008). For the LD coefficients, we used the interpolated values from Claret & Bloemen (2011). To model the stars, we used the Dartmouth stellar evolution tracks of Dotter et al. (2008) and the BT-SETTL stellar atmosphere models of Allard, Homeier & Freytag (2012) that we integrated in each individual bandpass. Since they are gravitationally bound, all stars were assumed to have the same metallicity and the same age. The orbits were assumed to be circular. We imposed that the physical companion is fainter by at least 1 mag in the $V$ band than the target star, otherwise, it would have been clearly identified in the spectral or CCF analysis. Each of the 16 light curves was modelled self-consistently allowing a different out-of-transit flux, contamination and an extra source of white noise (jitter). As PASTIS is not yet able to model the activity of stars in RV data, we decided not to use these extra constraints. We also modelled the spectral energy distribution of WASP-121 composed by the magnitudes in the Johnson-$B$ and -$V$, Sloan-$g'$, -$r'$, and -$i'$, 2-MASS $J$, $H$, and $K$s, and *WISE* $W1$ to $W4$ bandpasses from the APASS data base (Henden et al. 2015) and the AllWISE catalogue (Wright et al. 2010).

We analysed the aforementioned data using an MCMC procedure described in Díaz et al. (2014). For the priors, we used the results from the spectroscopic analysis (Section 3.1) for the parameters of the target star and the initial mass function from Kroupa (2001) for the blended stars. For the orbital ephemeris, we used normal priors matching the ephemeris reported in Table 4 with uncertainties boosted by 100, to avoid biasing the results with too narrow priors. For the other parameters, we chose uninformative priors. We limited the priors on the planet radius to be less than 2.2 $R_{\rm Jup}$, which is the radius of the biggest planet found so far: KOI-13 (Szabó et al. 2011). In PASTIS, planets are considered as non-self-emitting objects, hence no thermal emission. Only the reflected light is considered. Here, we used the albedo of the planet as a proxy for the depth of the occultation. The upper limit in the prior corresponds to a geometric albedo of 1 and a brightness temperature of 3500 K. The TRAPPIST photometry was performed on focus and no stellar contamination is detected within the photometric aperture. We thus defined a prior for the contamination centred on zero with an uncertainty of 1 per cent (positive and negative values are allowed) to account for possible variation of the sky background flux between the observations or for stellar brightness variation due to non-occulting spots. The EulerCam photometry was performed slightly out of focus, which means the target should be blended with the light from a ∼7.4 arcsec nearby star about 6.8 mag fainter ($R$ band), resulting in a contamination of 0.2 per cent. The prior for the EulerCam contamination was thus centred on this value. The exhaustive list of parameters and their priors are reported in Table A1. Both the planet and triple scenarios were described by 10 free parameters, while the planet in binary scenario used 11 free parameters. Among them, eight were in common (target star and orbital parameters). An additional 49 free parameters were needed to describe the data: three for each of the 16 light curves as already mentioned and an extrasource of white noise for the spectral energy distribution. For all scenarios, we ran 40 chains of $3.10^5$ iterations, randomly started from the joint prior distribution. All chains converged towards the same maximum of likelihood. We then thinned and merged the chains to derive the posterior distributions of all scenarios. They all have a posterior distribution with more than 1000 independent samples.

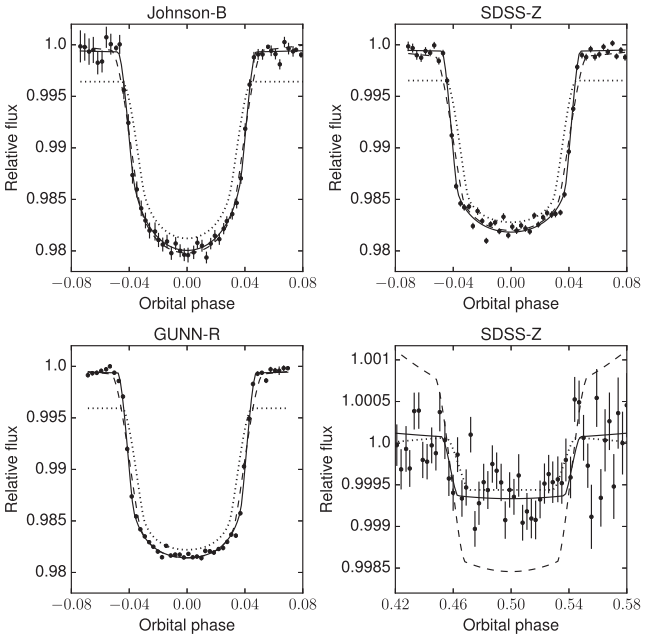


**Figure 11.** Phase-folded binned photometric data of WASP-121 observed in the various bandpasses together with the best planet (solid line), triple system (dash line), and planet in binary (dot line) models.

We report in Table A2 the median and 68.3 per cent confidence interval for the free parameters. All the fitted parameters for the planet scenario are compatible within $1\sigma$ with those derived in Section 3.3.

We display in Fig. 11 the transit and occultation data of WASP-121 in the various bandpasses together with the best planet, planet in binary and triple models. While the planet scenario reproduces well all the data, the triple system scenario is not able to fit perfectly the relatively sharp ingress and egress of the transit. The main difference between the two scenarios is for the secondary eclipse. While the planet scenario is able to reproduce well the occultation data, the best triple scenario exhibits a secondary depth of more than 2000 ppm, which is clearly excluded by the data. For the planet transiting a companion star to the target, it is not possible to reproduce the observed transit depth and duration if we assume both that the companion star is fainter by at least 1 mag than the target star and that the maximum planetary radius allowed is 2.2 $R_{\rm Jup}$. In these conditions, to reproduce well the transit data, the planet would need to have a radius of 3.24 $R_{\rm Jup}$, which is clearly unphysical for such objects.

We estimated the Bayes factor, $B_{ij}$, between the three scenarios using the method of Tuomi & Jones (2012). This method has some limitations that are discussed in Santerne et al. (2014). However, since we tested here scenarios that have nearly the same number of free parameters and most of these parameters have the same priors in the various scenarios, we assume that these limitations have no significant impact on our results. We found that $\log_{10}B_{ij} \sim 250$ and $\log_{10}B_{ij} \sim 870$, against the triple and planet-in-binary scenarios (respectively), in favour to the planet one. This significantly validates WASP-121 b as a *bona-fide* planet. Computing the BIC between the best models give a value of 1103 and 3905 against the triple and planet-in-binary scenarios (respectively), which confirms that WASP-121 b is a transiting planet.

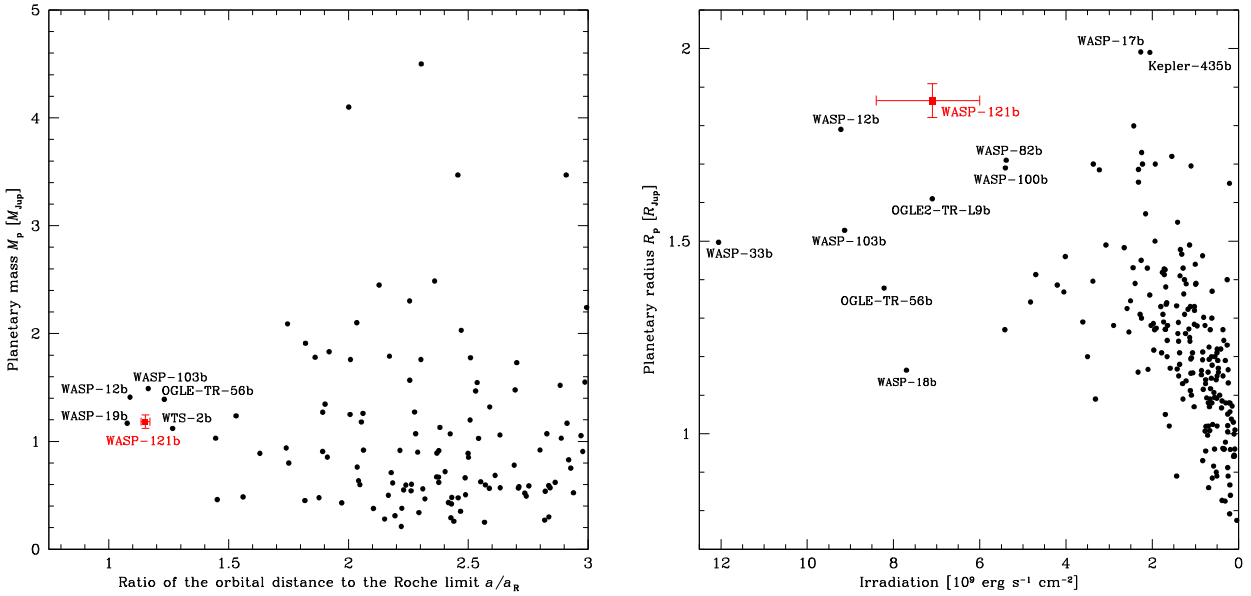


**Figure 12.** Left: orbital distance to the Roche limit ratio-mass diagram for the known transiting hot Jupiters with 0.2 $M_{Jup} < M_p < 13\ M_{Jup}$ and $P < 12$ d (data from the NASA Exoplanet Archive). We only show planets with $a/a_R < 3$. The planet WASP-121 b is shown in red. Right: irradiation-radius diagram for the same sample of planets.

## 5 DISCUSSION

WASP-121 b is a ∼1.18 $M_{Jup}$ planet in a 1.27 d orbit around a bright ($V = 10.4$) F6V star. Its most notable property is that its orbital semimajor axis is only ∼1.15 times larger than its Roche limit, which suggests that the planet is close to tidal disruption. Fig. 12 (left) shows the distribution of the orbital distance to the Roche limit ratio ($a/a_R$) as a function of the planetary mass for the known transiting planets with 0.2 $M_{Jup} < M_p < 13\ M_{Jup}$ and $P < 12$ d. WASP-121 b is one of the closest systems to tidal disruption, its direct competitors being WASP-12 b (Hebb et al. 2009), WASP-19 b (Hebb et al. 2010), WASP-103 b (Gillon et al. 2014), OGLE-TR-56 b (Konacki et al. 2003; Adams et al. 2011), and WTS-2 b (Birkby et al. 2014). According to Matsumura et al. (2010), these extreme planets are now expected to undergo tidal orbital decay through tidal dissipation inside the star only (we will elaborate on this in Section 5.2 in the case of WASP-121 b). The speed of this final orbital decay depends mainly on the mass of the planet and the tidal dissipation efficiency of the star. As noted by Gillon et al. (2014), the fact that all the planets near tidal disruption found to date have similar masses (between 1.1 and 1.5 $M_{Jup}$, see the left-hand panel of Fig. 12) could thus suggest a narrow range of tidal dissipation efficiencies for the host stars of the known transiting hot Jupiters (mainly solar-type stars).

### 5.1 Structural parameters of WASP-121 b: correction for asphericity using Roche geometry

Being close to its Roche limit, WASP-121 b might be significantly deformed by the intense tidal forces it is subject to (e.g. Budaj 2011) and even lose some of its mass through Roche lobe overflow (e.g. Lai, Helling & van den Heuvel 2010; Li et al. 2010). To evaluate the tidal distortion of the planet, we calculate its Roche shape by using the Roche model of Budaj (2011), as done by Southworth et al. (2015) for WASP-103 b. This model assumes that the planet is on a circular orbit and that it is rotating synchronously with its orbital period ($P_{rot} = P_{orb}$). This second assumption is perfectly reasonable as current theories of tidal evolution of close-in exoplanets predict synchronization times much shorter than times needed for circularization of the orbits (see e.g. Rasio & Ford 1996). The model takes as main inputs the orbital semimajor axis ($a = 5.47 \pm 0.11$ R$_\odot$), the star/planet mass ratio ($M_\star/M_p = 1198^{+141}_{-128}$), and the planetary radius ($R_p = 1.807 \pm 0.039\ R_{Jup}$), and computes the Roche shape of the planet which would have the same cross-section during the transit as the one we inferred from our observations assuming a spherical planet (eclipse model of Mandel & Agol 2002, see Section 3.3).

**Table 5.** Parameters describing the shape of WASP-121 b, obtained using the Roche model of Budaj (2011). The errors are the quadratic sum of the errors due to each input parameter ($a$, $M_\star/M_p$, and $R_p$).

| Parameter | Value |
|---|---|
| Radius at the substellar point $R_{sub}$ [$R_{Jup}$] | $2.009 \pm 0.072$ |
| Radius at the antistellar point $R_{back}$ [$R_{Jup}$] | $1.997 \pm 0.069$ |
| Radius at the rotation pole $R_{pole}$ [$R_{Jup}$] | $1.787 \pm 0.038$ |
| Radius on the side $R_{side}$ [$R_{Jup}$] | $1.828 \pm 0.041$ |
| Cross-sectional radius $R_{cross}$ [$R_{Jup}$] | $1.807 \pm 0.039$ |
| Mean radius $R_{mean}$ [$R_{Jup}$] | $1.865 \pm 0.044$ |
| Roche lobe filling parameter *ff* | $0.591 \pm 0.040$ |
| $R_{sub}/R_{side}$ | $1.099 \pm 0.020$ |
| $R_{sub}/R_{pole}$ | $1.124 \pm 0.026$ |
| $R_{side}/R_{pole}$ | $1.023 \pm 0.003$ |
| Density correction factor $(R_{cross}/R_{mean})^3$ | $0.910 \pm 0.013$ |

The results are displayed in Table 5. $R_{sub}$, $R_{back}$, $R_{pole}$, and $R_{side}$ are the planetary radii at the substellar point, the antistellar point, the rotation pole, and on the side, respectively. Together, these parameters describe the Roche shape of the planet. $R_{cross}$ is the cross-sectional radius, i.e. the radius of the sphere that would have the same cross-section as the Roche surface of the planet during the transit. It is the

planetary radius we derived from our global analysis in Section 3.3 (i.e. the observed radius). $R_{\rm mean}$ is the radius of the sphere with the same volume as the Roche surface of the planet. The Roche lobe filling parameter *ff* is defined as $R_{\rm sub}/R_{\rm L_1}$, where $R_{\rm L_1}$ is the distance of the Lagrangian L1 point. The asphericity of the planet can be quantified by the ratios $R_{\rm sub}/R_{\rm side}$, $R_{\rm sub}/R_{\rm pole}$, and $R_{\rm side}/R_{\rm pole}$. Finally, the quantity $(R_{\rm cross}/R_{\rm mean})^3$ is the *CF* that must be applied to the planetary density $\rho_{\rm p}$ derived from our global analysis assuming a spherical planet to convert it to the density obtained using the Roche model.

With a Roche lobe filling parameter of 0.59, WASP-121 b is still well away from Roche lobe overflow, despite being significantly deformed. It would none the less be interesting to search for potential signatures of planetary material surrounding WASP-121 (e.g. excess transit depths in the near-UV). Such signatures have indeed been possibly detected for WASP-12 by Fossati et al. (2010, 2013) and Haswell et al. (2012), although Budaj (2011) reported a value of only 0.61 for the Roche lobe filling parameter of WASP-12 b. If we use the $R_{\rm sub}/R_{\rm pole}$ ratio to quantify the departures from the sphere, we find that WASP-121 b ($R_{\rm sub}/R_{\rm pole} = 1.124$) is one of the most distorted planets known to date, alongside WASP-12 b ($R_{\rm sub}/R_{\rm pole} = 1.138$; Budaj 2011), WASP-19 b ($R_{\rm sub}/R_{\rm pole} = 1.124$; Budaj 2011), and WASP-103 b ($R_{\rm sub}/R_{\rm pole} = 1.120$; Southworth et al. 2015). This distortion is expected to produce characteristic signatures in the transit photometry of the system. There are two main features in the flux difference between the transit light curve of an ellipsoidal and a spherical planet (see Correia 2014 for details): an oscillation during the ingress and egress phases, and a 'bump' increase during the whole transit with a maximum value at the centre of the transit. For a giant planet close to its Roche limit such as WASP-121 b, these flux differences can reach 100 ppm (Correia 2014) and could thus be detected in ultraprecise transit photometry, obtained for example with the future missions CHEOPS (Broeg et al. 2013) and PLATO 2.0 (Rauer et al. 2014). This would allow us to estimate the fluid Love number (e.g. Love 1911) of the planet and to gain valuable insights on its internal structure.

$R_{\rm mean}$ being more representative of the physical size of the planet than $R_{\rm cross}$, we adopt it as our revised value for the planetary radius ($1.865 \pm 0.044\ R_{\rm Jup}$) and include it, as well as the subsequent revised value for the planetary density ($0.183 \pm 0.016\ \rho_{\rm Jup}$), in Table 4. We note that $R_{\rm mean}$ should be used when comparing the radius of the planet with theoretical models (e.g. Fortney, Marley & Barnes 2007), while $R_{\rm cross}$ should rather be employed when interpreting transmission or occultation data.

Several works showed that hot Jupiters' radii correlate well with their incident irradiation (see e.g. Demory & Seager 2011; Enoch, Collier Cameron & Horne 2012; Weiss et al. 2013). Fig. 12 (right) shows the position of WASP-121 b in an irradiation-radius diagram for the same sample of transiting planets as previously. With a radius of $1.865 \pm 0.044\ R_{\rm Jup}$ and an irradiation of $\sim 7.1\ 10^9$ erg s$^{-1}$ cm$^{-2}$, WASP-121 b joins the handful of extremely irradiated planets with superinflated radii. Its radius is actually significantly larger than the value of $1.50 \pm 0.03\ R_{\rm Jup}$ predicted by the equation derived by Weiss et al. (2013) from a sample of 103 transiting planets with a mass between 150 $M_\oplus$ and 13 $M_{\rm Jup}$ and that relates planets' sizes to their masses and irradiations. Several physical mechanisms have been proposed to explain the inflated radii of hot Jupiters, such as tidal heating (Bodenheimer, Lin & Mardling 2001), deposition of kinetic energy into the planets from strong winds driven by the large day/night temperature contrasts (Showman & Guillot 2002), enhanced atmospheric opacities (Burrows et al. 2007), reduced heat transport efficiency by layered convection inside the planets (Chabrier & Baraffe 2007), or Ohmic heating from currents induced through winds in the planetary atmospheres (Batygin & Stevenson 2010). As the WASP-121 system is quite young ($1.5 \pm 1.0$ Gyr, see Section 3.4), tidal circularization and dissipation might have occurred recently enough to contribute to the observed inflated radius.

### 5.2 Orbital evolution of WASP-121 b

In Section 3.3, we find a sky-projected spin-orbit angle of $\beta = 257\overset{\circ}{.}8^{+5\overset{\circ}{.}3}_{-5\overset{\circ}{.}5}$. This result suggests a significant misalignment between the spin axis of the host star and the orbital plane of the planet. Such a high misalignment could favour a migration of the planet involving strong dynamical events, such as planet–planet scattering (e.g. Rasio & Ford 1996; Weidenschilling & Marzari 1996; Moorhead & Adams 2005; Chatterjee et al. 2008) and/or Kozai–Lidov oscillations (e.g. Kozai 1962; Lidov 1962; Wu & Murray 2003; Fabrycky & Tremaine 2007). As shown in Fabrycky & Winn (2009), the true spin-orbit angle $\psi$, can be computed from $\beta$, $i_{\rm p}$ (the orbital inclination), and $i_\star$ (the stellar inclination). If we assume that the stellar rotation period $P_{\rm rot,\star}$ is either 0.89 d or 1.13 d and we combine this information with our measured values for $R_\star$ and $v_\star \sin i_\star$, we obtain $i_\star$ of $9\overset{\circ}{.}4 \pm 0\overset{\circ}{.}6$ and $11\overset{\circ}{.}9 \pm 0\overset{\circ}{.}7$, respectively (see Section 3.2). These values, together with our measured $\beta$ and $i_{\rm p}$, yield $\psi$ of $89\overset{\circ}{.}6 \pm 1\overset{\circ}{.}1$ and $90\overset{\circ}{.}1 \pm 1\overset{\circ}{.}2$, respectively, where the uncertainties are the quadratic sum of the uncertainties due to each input parameter. Both these solutions are in excellent agreement and would place the planet in a nearly polar orbit around its star, which would clearly be a remarkable configuration as noted by e.g. Lai (2012) and Rogers & Lin (2013).

The proximity of WASP-121 b to its Roche limit suggests that its orbital evolution is now dominated by tidal interactions with its host star. To assess the future orbital evolution of the planet, we integrate the tidal evolution equations of Matsumura et al. (2010) forwards in time, assuming that the planet is on a circular orbit (see Section 3.3) and that its rotation is now synchronized with its orbit. Under these reasonable assumptions, the planet's orbital evolution is expected to depend only on the tidal dissipation inside the star (Matsumura et al. 2010). The efficiency of this tidal dissipation is parametrized by the stellar tidal dissipation factor $Q'_\star$, with a higher $Q'_\star$ meaning a weaker tidal dissipation. We assume here that $Q'_\star \propto 1/|2\omega_\star - 2n|$, where $\omega_\star$ is the stellar angular velocity and $n$ is the planet's mean motion ($n = 2\pi/P$), as recommended by Matsumura et al. (2010) for the cases where the stellar rotation is not yet synchronized with the orbit (stellar rotation period $P_\star \neq P$). Under this assumption, $Q'_\star$ changes as $Q'_\star = Q'_0\ |2\omega_\star - 2n|/|2\omega_{\star,0} - 2n_0|$, where 0 index indicates the current values. Fig. 13 shows the obtained evolutions for the semimajor axis $a$ (top), the spin-orbit angle $\psi$ (middle), and the stellar rotation period $P_\star$ (bottom), assuming different values between $10^6$ and $10^9$ for the current stellar tidal dissipation factor $Q'_{\star,0}$ and a current stellar rotation period $P_{\star,0}$ of 0.89 d (left-hand panels) or 1.13 d (right-hand panels). For all cases, the model shows that the planet will continue to approach its host star until reaching its Roche limit, where it will be finally tidally disrupted. Assuming $P_{\star,0} = 0.89/1.13$ d, we find remaining lifetimes of 4.20/1.22 Myr, 42.0/12.2 Myr, 420/122 Myr, and 4.20/1.22 Gyr for $Q'_{\star,0}$ values of $10^6$, $10^7$, $10^8$, and $10^9$, respectively. We note that for $Q'_{\star,0} = 10^6$, the remaining lifetime of the planet would be <1 per cent of the youngest possible age of the system (500 Myr, see Section 3.4), thus giving a low probability for the planet to be detected now. This result could favour $Q'_{\star,0}$ values $\gtrsim 10^7$ for WASP-121, which would

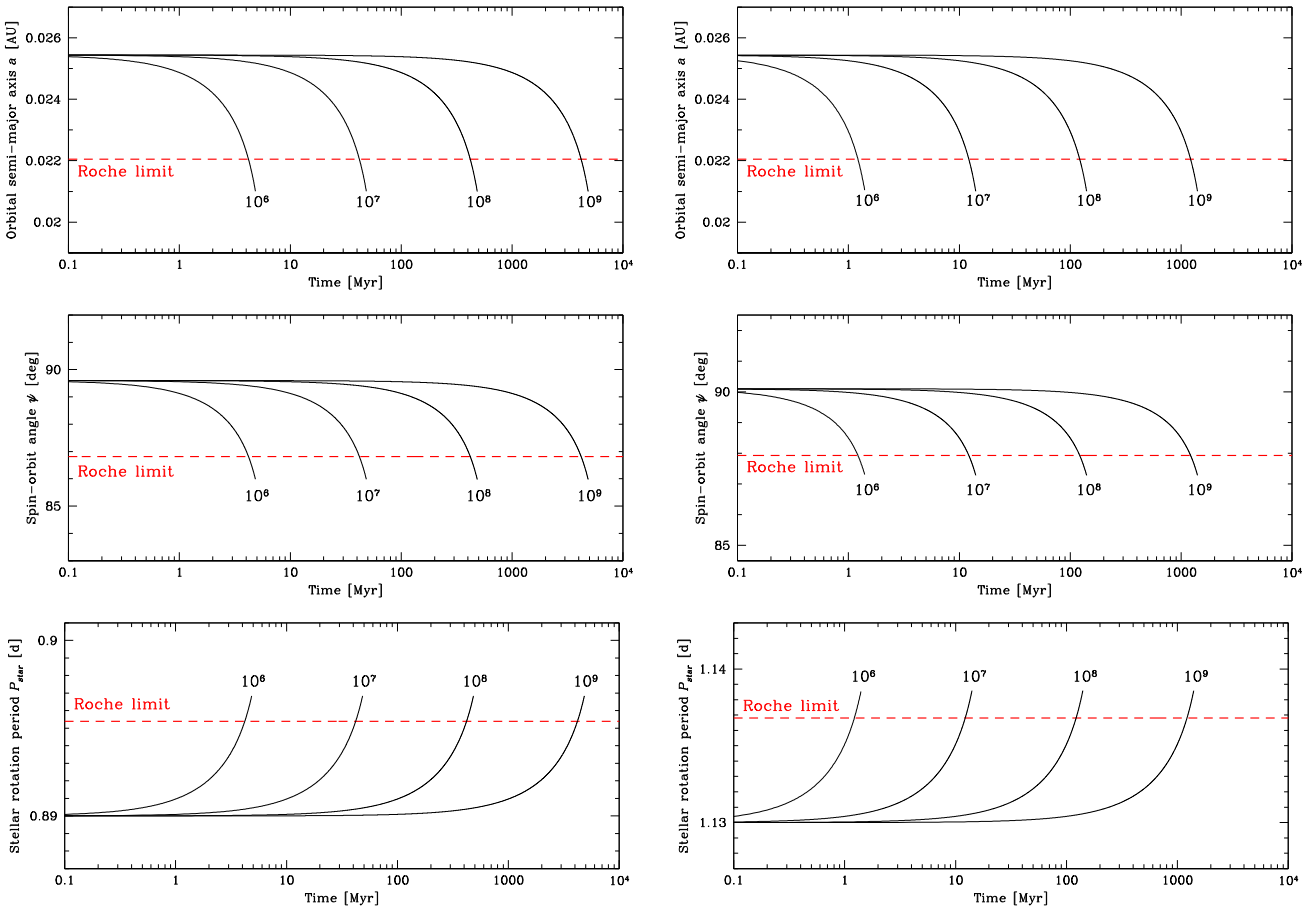


**Figure 13.** Future tidal evolution of the orbital semimajor axis (top), the spin-orbit angle (middle), and the stellar rotation period (bottom), assuming the current stellar rotation period $P_{\star,0}$ is 0.89 d (left-hand panels) or 1.13 d (right-hand panels). The labelled evolutions correspond to $Q'_{\star,0} = 10^6$, $10^7$, $10^8$, and $10^9$. The red horizontal dashed lines represent the Roche limit.

be in line with the expectation that hot stars ($T_{\rm eff} > 6250$ K) would have low tidal dissipation efficiencies due to their thin or quasi-non-existent convective envelopes (see e.g. Winn et al. 2010; Albrecht et al. 2012). For WASP-121, we have $T_{\rm eff} = 6460 \pm 140$ K and a thin convective envelope starting at 0.88 $R_\star$.

Combining the Matsumura et al.'s expression for d$a$/dt and the Kepler's third law, we can calculate the current rate of orbital period change: $({\rm d}P/{\rm dt})_0 = -0.0035\ (10^6/Q'_{\star,0})$ s yr$^{-1}$ for $P_{\star,0} = 0.89$ d and $({\rm d}P/{\rm dt})_0 = -0.0118\ (10^6/Q'_{\star,0})$ s yr$^{-1}$ for $P_{\star,0} = 1.13$ d. We can then estimate how long it would take to observe significant transit timing variations (TTVs) due to the orbital decay of the planet using, e.g. the equation 7 of Birkby et al. (2014). We note that this estimation assumes a constant rate of orbital period change d$P$/dt $= ({\rm d}P/{\rm dt})_0$. Fig. 14 shows the evolution of the shift in the transit time as a function of time for the different $Q'_{\star,0}$, and for $P_{\star,0} = 0.89$ d (top) or $P_{\star,0} = 1.13$ d (bottom). Assuming that a timing accuracy of ∼20 s is achievable with current instrumentation (see e.g. Gillon et al. 2009) and that $P_{\star,0} = 0.89/1.13$ d, TTVs could be detected at 3$\sigma$ after ∼11/6 yr for $Q'_{\star,0} = 10^6$, ∼35/19 yr for $Q'_{\star,0} = 10^7$, ∼110/60 yr for $Q'_{\star,0} = 10^8$, and ∼348/189 yr for $Q'_{\star,0} = 10^9$, respectively. For low values of $Q'_{\star,0}$, the decay of WASP-121 b's orbit could thus be detectable on the decade time-scale. Alternatively, the non-detection of TTVs in the WASP-121 b system after a certain amount of time would allow us to put a lower limit on $Q'_{\star,0}$ and help constrain tidal evolution theories.

### 5.3 Validity of the spherical approximation for the star WASP-121

The likely stellar rotation periods of 0.89 and 1.13 d would imply, together with our measured value for $R_\star$, rotation velocities $v_\star$ of 82.9 ± 1.7 and 65.3 ± 1.4 km s$^{-1}$, respectively (see Section 3.2). Such high $v_\star$ might imply a non-negligible deformation of the star due to its fast rotation. Using the Roche model from Maeder (2009), this deformation can be expressed as $R_{\star,\rm eq}/R_{\star,\rm pol} = 1 + (1/2)\ (\omega_\star/\omega_{\star,\rm K})^2$, where $\omega_\star$ is the rotation velocity; $\omega_{\star,\rm K}$ the critical break-up velocity; $R_{\star,\rm eq}$ the equatorial radius; and $R_{\star,\rm pol}$ the polar radius. We estimate the critical velocity from the Keplerian velocity $\sqrt{GM_\star/R^3_{\star,\rm eq}}$, for which the centrifugal force equals gravitational forces at the equator of the star. For WASP-121 (Table 4), $\omega_\star = 0.17\ \omega_{\star,\rm K}$, which gives $R_{\star,\rm eq}/R_{\star,\rm pol} = 1.015$. The deformation of the star induced by its possible rapid rotation would thus not strongly bias our stellar radius measurement (which has an error bar ∼2 per cent), even if it was obtained assuming a spherical shape for the star (eclipse model of Mandel & Agol 2002, see Section 3.3).

### 5.4 First constraints on the atmospheric properties of WASP-121 b

The large radius of WASP-121 b, its extreme irradiation, and the brightness of its host star make it an excellent target for atmospheric

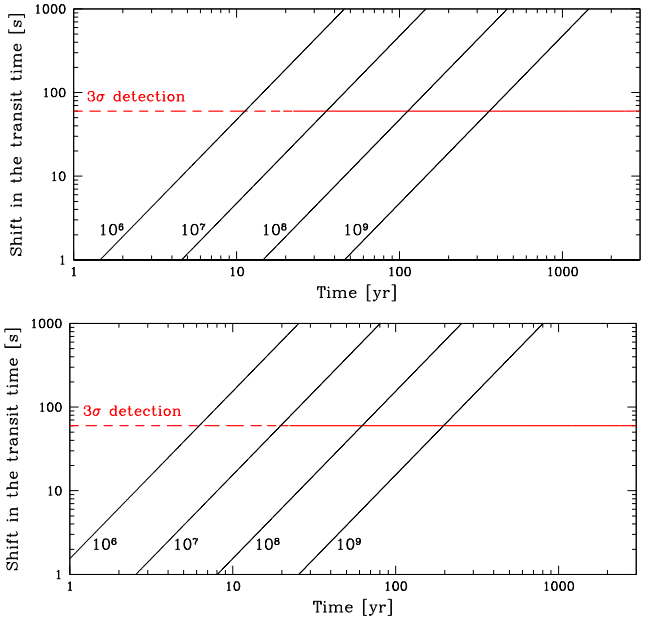


**Figure 14.** Shift in the transit time of WASP-121 b as a function of time, computed for different values of $Q'_{\star,0}$, assuming the current stellar rotation period is 0.89 d (top) or 1.13 d (bottom). The labelled evolutions correspond to $Q'_{\star,0} = 10^6$, $10^7$, $10^8$, and $10^9$. The red horizontal line represents the $3\sigma$ detection limit, assuming a timing accuracy of 20 s.

studies via secondary eclipse observations, with theoretical expectations for the planet-to-star IR flux ratio >0.05 per cent down to ∼0.9 μm.

By combining seven occultation light curves obtained with TRAPPIST, we detect the emission of the planet in the $z'$ band at better than $\sim 4\sigma$, the measured occultation depth being 603 ± 130 ppm (see Fig. 5). To make sure that the detected signal does not result from a systematic effect present in one or several light curves, we followed the method presented in Lendl et al. (2013). We thus divided our set of seven occultation light curves into subsets containing all possible combinations of three to six light curves and performed an MCMC analysis on each of them, while keeping all the jump parameters except the occultation depth fixed to the values derived from our global analysis (Table 4). Fig. 15 presents histograms of the derived occultation depths. We can see how the solutions converge towards our adopted value as we use an increasing number of occultation light curves.

Our measured occultation depth can be translated into a brightness temperature $T_{\rm br}$ of $3553^{+160}_{-178}$ K. In this calculation, we considered the planet as a blackbody of temperature $T_{\rm br}$ and used a Kurucz model spectrum for the star (Castelli & Kurucz 2004). We also assumed that all the planet's $z'$-band flux arises from thermal emission, which is reasonable as López-Morales & Seager (2007) showed that reflected light contributes 10 to 20 times less than thermal emission at these wavelengths for very hot Jupiters, such as WASP-121 b. We then defined our measured occultation depth as the product of the planet-to-star area ratio and the ratio of the TRAPPIST $z'$ bandpass-integrated planet-to-star fluxes (e.g. Charbonneau et al. 2005), and adopted as brightness temperature the blackbody temperature that yielded the best match to our measured occultation depth. The uncertainty on $T_{\rm br}$ only accounts for the uncertainty on the measured occultation depth, which is the main source of error.

We can compare this brightness temperature to the equilibrium temperature of the planet, which is given by $T_{\rm eq} = T_{\rm eff}\sqrt{R_\star/a}\ [f\,(1 - A_{\rm B})]^{1/4}$, where $f$ and $A_{\rm B}$ are the reradiation factor and the Bond albedo of the planet, respectively (López-Morales & Seager 2007). The factor $f$ ranges from 1/4 to 2/3, where $f = 1/4$ indicates efficient heat redistribution and isotropic reradiation over the whole planet and $f = 2/3$ corresponds to instantaneous reradiation of incident radiation with no heat redistribution. The brightness temperature is significantly higher ($\sim 7\sigma$) than the maximum equilibrium temperature of $3013^{+77}_{-75}$ K obtained assuming $A_{\rm B} = 0$ and $f = 2/3$, which could suggest that the planet has a low Bond albedo coupled to a poor heat redistribution efficiency. This would agree with the trend noted by Cowan & Agol (2011) that hottest planets are less efficient at redistributing the incident stellar energy than colder planets, the explanation proposed for this trend being that the radiative time-scale is shorter than the advective time-scale for hotter planets, causing these planets to reradiate the incident stellar energy rather than advecting it through winds.

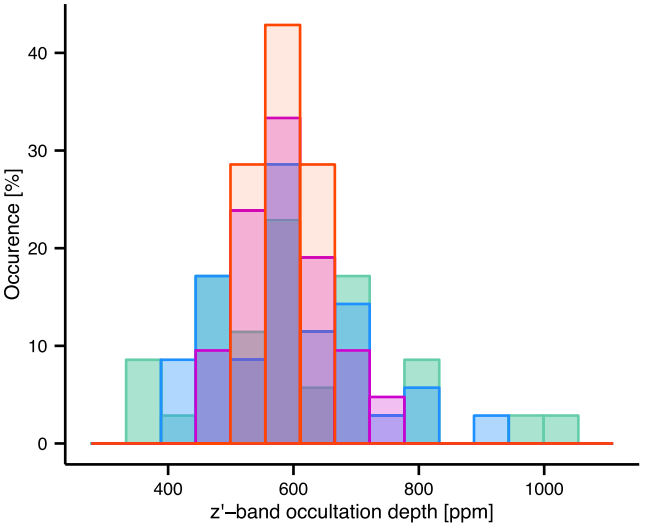


**Figure 15.** Histograms of the $z'$-band occultation depths derived from the MCMC analyses of subsets of three (green), four (blue), five (purple), and six (red) light curves chosen among the seven TRAPPIST occultation light curves.

However, we note that the comparison of brightness temperature with equilibrium temperature has only limited physical meaning here as our $z'$-band observations probe thermal emission from deep layers ($P \sim 1$ bar) of the planetary atmosphere, that can be hotter than the maximum equilibrium temperature (e.g. Madhusudhan 2012). Furthermore, the emission spectrum of a hot Jupiter can deviate significantly from that of a blackbody. For instance, the flux observed in the $z'$ band can be noticeably increased (respectively, decreased) by emission (respectively, absorption) due to gaseous TiO, which is expected to be abundant if the atmosphere has a carbon-to-oxygen (C/O) ratio <1 (O-rich atmosphere).[6]

Our $z'$-band occultation measurement thus provides a first observational constraint on the emission spectrum of WASP-121 b. Combined with future observations at longer wavelengths (from the ground in the near-infrared $J$, $H$, and $K$ bands, or from space between 1.1 and 1.7 μm with *HST*/WFC3 or at 3.6 and 4.5 μm with *Spitzer*/IRAC), it will allow us to gain insights on the planet's dayside chemical composition and thermal structure.

[6] Whether TiO is seen in emission or absorption in that case depends on the thermal structure of the planetary atmosphere (presence or lack of temperature inversion; see Madhusudhan 2012 for details).

## ACKNOWLEDGEMENTS

We would like to thank G. Buldgen, A. Correia, B.-O. Demory, and X. Dumusque for their valuable suggestions. WASP-South is hosted by the SAAO and we are grateful for their ongoing support and assistance. Funding for WASP comes from consortium universities and from UK's Science and Technology Facilities Council. TRAPPIST is a project funded by the Belgian Fund for Scientific Research (Fonds National de la Recherche Scientifique, F.R.S.-FNRS) under grant FRFC 2.5.594.09.F, with the participation of the Swiss National Science Fundation (SNF). The Swiss *Euler* Telescope is operated by the University of Geneva, and is funded by the Swiss National Science Foundation. LD acknowledges support of the F.R.I.A. fund of the FNRS. MG, EJ and VVG are FNRS Research Associates. ML acknowledges support of the European Research Council through the European Union's Seventh Framework Programme (FP7/2007-2013)/ERC grant agreement number 336480. AHMJT received funding from a fellowship provided by the Swiss National Science Foundation under grant number P300P2-147773. AS is supported by the European Union under a Marie Curie Intra-European Fellowship for Career Development with reference FP7-PEOPLE-2013-IEF, number 627202. We thank the anonymous referee for her/his valuable suggestions. The photometric and RV time series used in this work are publicly available at the CDS via anonymous ftp to cdsarc.u-strasbg.fr.

## REFERENCES

Adams E. R. et al., 2011, ApJ, 741, 102
Albrecht S. et al., 2012, ApJ, 757, 18
Allard F., Homeier D., Freytag B., 2012, in Richards M. T., Hubeny I., eds, Proc. IAU Symp. 282, rom Interacting Binaries to Exoplanets: Essential Modeling Tools. Kluwer, Dordrecht, p. 235
Anderson D. R. et al., 2013, MNRAS, 430, 3422
Anderson D. R. et al., 2014, preprint (arXiv:1410.3449)
Andretta V., Giampapa M. S., 1995, ApJ, 439, 405
Asplund M., Grevesse N., Sauval A. J., Scott P., 2009, ARA&A, 47, 481
Bakos G., Noyes R. W., Kovács G., Stanek K. Z., Sasselov D. D., Domsa I., 2004, PASP, 116, 266
Baranne A. et al., 1996, A&AS, 119, 373
Batygin K., Stevenson D. J., 2010, ApJ, 714, L238
Birkby J. L. et al., 2014, MNRAS, 440, 1470
Bodenheimer P., Lin D. N. C., Mardling R. A., 2001, ApJ, 548, 466
Böhm-Vitense E., 2004, AJ, 128, 2435
Borsa F. et al., 2015, A&A, 578, A64
Broeg C. et al., 2013, in Saglia R., ed., EPJ Web Conf., 47, Hot Planets and Cool Stars. EDP Sciences, p. 3005
Budaj J., 2011, AJ, 141, 59
Burrows A., Hubeny I., Budaj J., Hubbard W. B., 2007, ApJ, 661, 502
Castelli F., Kurucz R. L., 2004, preprint (astro-ph/0405087)
Chabrier G., Baraffe I., 2007, ApJ, 661, L81
Chandrasekhar S., 1987, Ellipsoidal Figures of Equilibrium. Dover, New York
Charbonneau D. et al., 2005, ApJ, 626, 523
Chatterjee S., Ford E. B., Matsumura S., Rasio F. A., 2008, ApJ, 686, 580
Claret A., Bloemen S., 2011, A&A, 529, A75
Collier Cameron A. et al., 2006, MNRAS, 373, 799
Collier Cameron A. et al., 2007, MNRAS, 380, 1230
Correia A. C. M., 2014, A&A, 570, L5
Cowan N. B., Agol E., 2011, ApJ, 729, 54
Cumming A., 2010, in Seager S., ed., Exoplanets. Univ. Arizona Press, Tucson, AZ, p. 191
Demory B.-O., Seager S., 2011, ApJS, 197, 12
Díaz R. F., Almenara J. M., Santerne A., Moutou C., Lethuillier A., Deleuil M., 2014, MNRAS, 441, 983
Dotter A., Chaboyer B., Jevremović D., Kostov V., Baron E., Ferguson J. W., 2008, ApJS, 178, 89
Doyle A. P. et al., 2013, MNRAS, 428, 3164
Doyle A. P., Davies G. R., Smalley B., Chaplin W. J., Elsworth Y., 2014, MNRAS, 444, 3592
Dravins D., Lindegren L., Nordlund A., 1981, A&A, 96, 345
Dumusque X., Boisse I., Santos N. C., 2014, ApJ, 796, 132
Enoch B., Collier Cameron A., Horne K., 2012, A&A, 540, A99
Etzel P. B., 1981, in Carling E. B., Kopal Z., eds, Photometric and Spectroscopic Binary Systems. Reidel, Dordrecht, p. 111
Fabrycky D., Tremaine S., 2007, ApJ, 669, 1298
Fabrycky D. C., Winn J. N., 2009, ApJ, 696, 1230
Ford E. B., Rasio F. A., 2006, ApJ, 638, L45
Fortney J. J., Marley M. S., Barnes J. W., 2007, ApJ, 659, 1661
Fossati L. et al., 2010, ApJ, 714, L222
Fossati L., Ayres T. R., Haswell C. A., Bohlender D., Kochukhov O., Flöer L., 2013, ApJ, 766, L20
Gelman A., Rubin D., 1992, Stat. Sci., 7, 457
Gillon M. et al., 2009, A&A, 496, 259
Gillon M. et al., 2010, A&A, 511, A3
Gillon M., Jehin E., Magain P., Chantry V., Hutsemékers D., Manfroid J., Queloz D., Udry S., 2011, in Bouchy F., Díaz R., Moutou C., eds, EPJ Web Conf. 11, Detection and Dynamics of Transiting Exoplanets. EDP Sciences, p. 6002
Gillon M. et al., 2012, A&A, 542, A4
Gillon M. et al., 2014, A&A, 562, L3
Giménez A., 2006, ApJ, 650, 408
Goldreich P., Tremaine S., 1980, ApJ, 241, 425
Gray D. F., 2008, The Observation and Analysis of Stellar Photospheres. Cambridge Univ. Press, Cambridge
Guillochon J., Ramirez-Ruiz E., Lin D., 2011, ApJ, 732, 74
Hartman J. D. et al., 2011, ApJ, 742, 59
Haswell C. A. et al., 2012, ApJ, 760, 79
Hebb L. et al., 2009, ApJ, 693, 1920
Hebb L. et al., 2010, ApJ, 708, 224
Hellier C. et al., 2011, in Bouchy F., Díaz R., Moutou C., eds, EPJ Web Conf. 11, Detection and Dynamics of Transiting Exoplanets. EDP Sciences, p. 1004
Hellier C. et al., 2012, MNRAS, 426, 739
Henden A. A., Levine S., Terrell D., Welch D. L., 2015, BAAS, 225, 336.16
Holman M. J. et al., 2006, ApJ, 652, 1715
Howard A. W. et al., 2012, ApJS, 201, 15
Izotov Y. I., Thuan T. X., 2010, ApJ, 710, L67
Jackson B., Greenberg R., Barnes R., 2008, ApJ, 678, 1396
Jehin E. et al., 2011, The Messenger, 145, 2
Jenkins J. S., Tuomi M., 2014, ApJ, 794, 110
Konacki M., Torres G., Jha S., Sasselov D. D., 2003, Nature, 421, 507
Kordopatis G. et al., 2013, AJ, 146, 134
Kovács G., Zucker S., Mazeh T., 2002, A&A, 391, 369
Kozai Y., 1962, AJ, 67, 591
Kroupa P., 2001, MNRAS, 322, 231
Lai D., 2012, MNRAS, 423, 486
Lai D., Helling C., van den Heuvel E. P. J., 2010, ApJ, 721, 923
Lendl M. et al., 2012, A&A, 544, A72
Lendl M., Gillon M., Queloz D., Alonso R., Fumel A., Jehin E., Naef D., 2013, A&A, 552, A2
Lidov M. L., 1962, Planet. Space Sci., 9, 719
Li S.-L., Miller N., Lin D. N. C., Fortney J. J., 2010, Nature, 463, 1054
Lin D. N. C., Papaloizou J., 1986, ApJ, 309, 846
López-Morales M., Seager S., 2007, ApJ, 667, L191
Love A. E. H., 1911, Some Problems of Geodynamics. Cambridge Univ. Press, Cambridge
Lubow S. H., Ida S., 2010, in Seager S., ed., Planet Migration. Univ. Arizona Press, Tucson, AZ, p. 347

McLaughlin D. B., 1924, ApJ, 60, 22
Madhusudhan N., 2012, ApJ, 758, 36
Maeder A., 2009, in Börner G. et al., eds, Astronomy and Astrophysics Library, Physics, Formation and Evolution of Rotating Stars. Springer, Berlin, p. 19
Magain P., 1984, A&A, 134, 189
Mandel K., Agol E., 2002, ApJ, 580, L171
Marcy G. W., Butler R. P., Fischer D. A., Vogt S. S., 2004, in Beaulieu J., Lecavelier Des Etangs A., Terquem C., eds, ASP Conf. Ser. Vol. 321, Extrasolar Planets: Today and Tomorrow. Astron. Soc. Pac., San Francisco, p. 501
Matsumura S., Peale S. J., Rasio F. A., 2010, ApJ, 725, 1995
Maxted P. F. L. et al., 2011, PASP, 123, 547
Mayor M. et al., 2011, preprint (arXiv:1109.2497)
Meibom S. et al., 2013, Nature, 499, 55
Melo C. et al., 2007, A&A, 467, 721
Moorhead A. V., Adams F. C., 2005, Icarus, 178, 517
Morton T. D., Johnson J. A., 2011, ApJ, 738, 170
Murray C. D., Correia A. C. M., 2010, in Seager S., ed., Keplerian Orbits and Dynamics of Exoplanets. Univ. Arizona Press, Tucson, AZ, p. 15
Nelson B., Davis W. D., 1972, ApJ, 174, 617
Noels A., Montalbán J., 2013, in Shibahashi H., Lynas-Gray A. E., eds, ASP Conf. Ser. Vol. 479, Progress in Physics of the Sun and Stars: A New Era in Helio- and Asteroseismology. Astron. Soc. Pac., San Francisco, p. 435
Noyes R. W., Hartmann L. W., Baliunas S. L., Duncan D. K., Vaughan A. H., 1984, ApJ, 279, 763
Ogilvie G. I., 2009, MNRAS, 396, 794
Penev K., Jackson B., Spada F., Thom N., 2012, ApJ, 751, 96
Pepe F., Mayor M., Galland F., Naef D., Queloz D., Santos N. C., Udry S., Burnet M., 2002, A&A, 388, 632
Pollacco D. L. et al., 2006, PASP, 118, 1407
Popper D. M., Etzel P. B., 1981, AJ, 86, 102
Queloz D. et al., 2000, A&A, 354, 99
Queloz D. et al., 2001, A&A, 379, 279
Raghavan D. et al., 2010, ApJS, 190, 1
Rasio F. A., Ford E. B., 1996, Science, 274, 954
Rauer H. et al., 2014, Exp. Astron., 38, 249
Rogers T. M., Lin D. N. C., 2013, ApJ, 769, L10
Rossiter R. A., 1924, ApJ, 60, 15
Santerne A. et al., 2014, A&A, 571, A37
Santerne A. et al., 2015, MNRAS, 451, 2337
Santos N. C. et al., 2002, A&A, 392, 215
Scargle J. D., 1982, ApJ, 263, 835
Schwarz G. E., 1978, Ann. Statist., 6, 461
Scuflaire R., Théado S., Montalbán J., Miglio A., Bourge P.-O., Godart M., Thoul A., Noels A., 2008, Ap&SS, 316, 83
Seager S., Deming D., 2010, ARA&A, 48, 631
Seager S., Mallén-Ornelas G., 2003, ApJ, 585, 1038
Showman A. P., Guillot T., 2002, A&A, 385, 166
Southworth J., 2008, MNRAS, 386, 1644
Southworth J. et al., 2015, MNRAS, 447, 711
Stetson P. B., 1987, PASP, 99, 191
Szabó G. M. et al., 2011, ApJ, 736, L4
Tamuz O., Mazeh T., Zucker S., 2005, MNRAS, 356, 1466
Tanaka H., Takeuchi T., Ward W. R., 2002, ApJ, 565, 1257
Torres G., Konacki M., Sasselov D. D., Jha S., 2005, ApJ, 619, 558
Torres G., Andersen J., Giménez A., 2010, A&AR, 18, 67
Triaud A. H. M. J. et al., 2010, A&A, 524, A25
Triaud A. H. M. J. et al., 2011, A&A, 531, A24
Tuomi M., Jones H. R. A., 2012, A&A, 544, A116
Tuomi M., Anglada-Escude G., Jenkins J. S., Jones H. R. A., 2014, preprint (arXiv:1405.2016)
Weidenschilling S. J., Marzari F., 1996, Nature, 384, 619
Weiss L. M. et al., 2013, ApJ, 768, 14
Winn J. N., 2010, in Seager S., ed., Transits and Occultations, Exoplanets. Univ. Arizona Press, Tucson, AZ, p. 55
Winn J. N., Fabrycky D., Albrecht S., Johnson J. A., 2010, ApJ, 718, L145
Wright E. L. et al., 2010, AJ, 140, 1868
Wu Y., Murray N., 2003, ApJ, 589, 605

## APPENDIX A: PASTIS MCMC ANALYSIS OF THE PHOTOMETRIC DATA

**Table A1.** Priors used in the PASTIS analyses: $\mathcal{U}(a;b)$ represents a Uniform prior between $a$ and $b$; $\mathcal{N}(\mu;\sigma^2)$ represents a normal distribution with a mean of $\mu$ and a width of $\sigma^2$; $\mathcal{P}(\alpha;x_{\rm min};x_{\rm max})$ represents a power-law distribution with an exponent $\alpha$ computed between $x_{\rm min}$ and $x_{\rm max}$ ; $\mathcal{P}_2(\alpha_1;\alpha_2;x_0;x_{\rm min};x_{\rm max})$ represents a double power-law distribution with an exponent $\alpha_1$ computed between $x_{\rm min}$ and $x_0$ and an exponent $\alpha_2$ computed between $x_0$ and $x_{\rm max}$; and finally $\mathcal{S}(a;b)$ represents a Sine distribution between $a$ and $b$.

| Parameter | Planet | Planet in binary | Triple |
|---|---|---|---|
| *Target parameters* | | | |
| Effective temperature $T_{\rm eff}$ [K] | $\mathcal{N}(6460;140)$ | $\mathcal{N}(6460;140)$ | $\mathcal{N}(6460;140)$ |
| Surface gravity $\log g$ [cm.s$^{-2}$] | $\mathcal{N}(4.2;0.2)$ | $\mathcal{N}(4.2;0.2)$ | $\mathcal{N}(4.2;0.2)$ |
| Iron abundance [Fe/H] [dex] | $\mathcal{N}(0.13;0.09)$ | $\mathcal{N}(0.13;0.09)$ | $\mathcal{N}(0.13;0.09)$ |
| Distance $d$ [pc] | $\mathcal{P}(2.0;10;10000)$ | $\mathcal{P}(2.0;10;10000)$ | $\mathcal{P}(2.0;10;10000)$ |
| Interstellar extinction $E(B-V)$ [mag] | $\mathcal{U}(0;0.1)$ | $\mathcal{U}(0;0.1)$ | $\mathcal{U}(0;0.1)$ |
| *Planet parameters* | | | |
| Radius $R_p$ [$R_{\rm jup}$] | $\mathcal{U}(0;2.2)$ | $\mathcal{U}(0;2.2)$ | – |
| Albedo $A_g$ | $\mathcal{U}(0;2.5)$ | $\mathcal{U}(0;2.5)$ | – |
| *Binary parameters* | | | |
| Mass of stellar host $M_2$ [$M_\odot$] | – | $\mathcal{P}_2(-1.3;-2.3;0.5;0.1;2)$ | $\mathcal{P}_2(-1.3;-2.3;0.5;0.1;2)$ |
| Mass of stellar companion $M_3$ [$M_\odot$] | – | – | $\mathcal{P}_2(-1.3;-2.3;0.5;0.1;2)$ |
| *Orbital parameters* | | | |
| Orbital period $P$ [d] | $\mathcal{N}(1.274\,9255;5.10^{-4})$ | $\mathcal{N}(1.274\,9255;5.10^{-4})$ | $\mathcal{N}(1.274\,9255;5.10^{-4})$ |
| Transit epoch $T_0$ [BJD – 2450000] | $\mathcal{N}(6635.70832;0.03)$ | $\mathcal{N}(6635.70832;0.03)$ | $\mathcal{N}(6635.70832;0.03)$ |
| Orbital inclination $i$ [°] | $\mathcal{S}(60;90)$ | $\mathcal{S}(60;90)$ | $\mathcal{S}(60;90)$ |
| *TRAPPIST data parameters* ($\times$ 12) | | | |
| Contamination | $\mathcal{N}(0;0.01)$ | $\mathcal{N}(0;0.01)$ | $\mathcal{N}(0;0.01)$ |
| Out-of-transit flux | $\mathcal{U}(0.9;1.1)$ | $\mathcal{U}(0.9;1.1)$ | $\mathcal{U}(0.9;1.1)$ |
| Jitter | $\mathcal{U}(0;0.1)$ | $\mathcal{U}(0;0.1)$ | $\mathcal{U}(0;0.1)$ |
| *EulerCam data parameters* ($\times$ 4) | | | |
| Contamination | $\mathcal{N}(0.002;0.01)$ | $\mathcal{N}(0.002;0.01)$ | $\mathcal{N}(0.002;0.01)$ |
| Out-of-transit flux | $\mathcal{U}(0.9;1.1)$ | $\mathcal{U}(0.9;1.1)$ | $\mathcal{U}(0.9;1.1)$ |
| Jitter | $\mathcal{U}(0;0.1)$ | $\mathcal{U}(0;0.1)$ | $\mathcal{U}(0;0.1)$ |
| *Spectral energy distribution parameter* | | | |
| Jitter [mag] | $\mathcal{U}(0;1)$ | $\mathcal{U}(0;1)$ | $\mathcal{U}(0;1)$ |

**Table A2.** Posterior distributions results of the PASTIS analyses.

| Parameter | Planet | Planet in binary | Triple |
|---|---|---|---|
| *Target parameters* | | | |
| Effective temperature $T_{\rm eff}$ [K] | $6650 \pm 60$ | $6140 \pm 150$ | $6763^{+46}_{-160}$ |
| Surface gravity $\log g$ [cm.s$^{-2}$] | $4.245 \pm 0.006$ | $3.949^{+0.031}_{-0.014}$ | $3.770^{+0.002}_{-0.004}$ |
| Iron abundance [Fe/H] [dex] | $0.1 \pm 0.1$ | $-0.51^{+0.01}_{-0.22}$ | $-0.21^{+0.05}_{-0.01}$ |
| Distance $d$ [pc] | $261 \pm 4.6$ | $334 \pm 12$ | $578^{+7}_{-10}$ |
| Interstellar extinction $E(B-V)$ [mag] | $0.009^{+0.012}_{-0.007}$ | $0.0077^{+0.014}_{-0.006}$ | $0.048^{+0.014}_{-0.029}$ |
| *Planet parameters* | | | |
| Radius $R_p$ [$R_{\rm jup}$] | $1.76 \pm 0.02$ | $2.1998^{+0.0001}_{-0.0005}$ | – |
| Albedo $A_g$ | $0.55 \pm 0.12^a$ | $1.14 \pm 0.18^b$ | – |
| *Binary parameters* | | | |
| Mass of eclipse host $M_2$ [$M_\odot$] | – | $0.947 \pm 0.007^c$ | $1.41^{+0.01\,c}_{-0.03}$ |
| Mass of eclipse companion $M_3$ [$M_\odot$] | – | – | $0.367^{+0.003\,c}_{-0.008}$ |
| *Orbital parameters* | | | |
| Orbital period $P$ [d] | $1.274\,924\,77 \pm 5.4\ 10^{-7}$ | $1.274\,9280 \pm 1.7\ 10^{-6}$ | $1.274\,924\,95 \pm 7.4\ 10^{-7}$ |
| Transit epoch $T_0$ [BJD – 2450000] | $6635.7077 \pm 0.0001$ | $6635.7077 \pm 0.0034$ | $6635.7077 \pm 0.0002$ |
| Orbital inclination $i$ [°] | $89.13^{+0.60}_{-0.94}$ | $89.90 \pm 0.09$ | $89.78^{+0.16}_{-0.23}$ |
| *Spectral energy distribution parameter* | | | |
| Jitter [mag] | $0.013 \pm 0.013$ | $0.170 \pm 0.072$ | $0.014^{+0.014}_{-0.009}$ |

*Notes.* [a]This corresponds to an occultation depth of $620 \pm 140$ ppm.
[b]This corresponds to an occultation depth of $2470 \pm 370$ ppm.
[c]The error does not account for the uncertainty of the stellar models.

This paper has been typeset from a TEX/LATEX file prepared by the author.